Journal of Volcanology and Geothermal Research 419 (2021) 107354

Contents lists available at ScienceDirect

Journal of Volcanology and Geothermal Research

journal homepage: www.elsevier.com/locate/jvolgeores

Invited research article

Evaluating the state-of-the-art in remote volcanic eruption characterization Part I: Raikoke volcano, Kuril Islands

Kathleen McKee [a,b,*], Cassandra M. Smith [c], Kevin Reath [d], Eveanjelene Snee [e], Sean Maher [f], Robin S. Matoza [f], Simon Carn [g], Larry Mastin [h], Kyle Anderson [i], David Damby [i], Diana C. Roman [a], Artem Degterev [j], Alexander Rybin [j], Marina Chibisova [j], Jelle D. Assink [k], Rodrigo de Negri Leiva [f,l], Anna Perttu [m]

[a] Earth and Planets Laboratory, Carnegie Institution for Science, Washington, DC, USA
[b] Los Alamos National Laboratory, Los Alamos, NM, USA
[c] Alaska Volcano Observatory, U.S. Geological Survey, Anchorage, AK, USA
[d] Department of Earth and Atmospheric Sciences, Cornell University, Ithaca, NY, USA
[e] School of Earth and Environmental Scienes, Cardiff University, Cardiff, Wales, UK
[f] Department of Earth Science and Earth Research Institute, University of California, Santa Barbara, Santa Barbara, CA, USA
[g] Department of Geological and Mining Engineering and Sciences, Michigan Technological University, Houghton, MI, USA
[h] U.S.Geological Survey Cascades Volcano Observatory, Vancouver, WA, USA
[i] U.S. Geological Survey, California Volcano Observatory, Moffett Field, CA, USA
[j] Sakhalin Volcanic Eruptions Response Team (SVERT), Institute of Marine Geology and Geophysics, Yuzhno-Sakhalinsk, Russia
[k] R&D Seismology and Acoustics, Royal Netherlands Meteorological Institute (KNMI), De Bilt, the Netherlands
[l] NDC-CTBT of the Chilean Nuclear Energy Commission, Chile
[m] Earth Observatory of Singapore, Nanyang Technological University, Singapore

ARTICLE INFO

Article history:
Received 9 January 2021
Received in revised form 16 July 2021
Accepted 19 July 2021
Available online 24 July 2021

Keywords:
Volcanic eruption characterization
Satellite remote sensing
Infrasound
Lightning
Plume modeling
Raikoke Volcano

ABSTRACT

Raikoke, a small, unmonitored volcano in the Kuril Islands, erupted in June 2019. We integrate data from satellites (including Sentinel-2, TROPOMI, MODIS, Himawari-8), the International Monitoring System (IMS) infrasound network, and global lightning detection network (GLD360) with information from local authorities and social media to retrospectively characterize the eruptive sequence and improve understanding of the pre-, *syn*- and post- eruptive behavior. We observe six infrasound pulses beginning on 21 June at 17:49:55 UTC as well as the main Plinian phase on 21 June at 22:29 UTC. Each pulse is tracked in space and time using lightning and satellite imagery as the plumes drift eastward. Post-eruption visible satellite imagery shows expansion of the island's surface area, an increase in crater size, and a possibly-linked algal bloom south of the island. We use thermal satellite imagery and plume modeling to estimate plume height at 10–12 km asl and 1.5–2 × 10^6 kg/s mass eruption rate. Remote infrasound data provide insight into *syn*-eruptive changes in eruption intensity. Our analysis illustrates the value of interdisciplinary analyses of remote data to illuminate eruptive processes. However, our inability to identify deformation, pre-eruptive outgassing, and thermal signals, which may reflect the relatively short duration (~12 h) of the eruption and minimal land area around the volcano and/or the character of closed-system eruptions, highlights current limitations in the application of remote sensing for eruption detection and characterization.

1. Introduction

Many volcanoes around the world lack dedicated, local ground-based instrumentation. At those that do host ground-based instrumentation it comes with significant challenges to maintain, especially at remote volcanoes, and is often destroyed during the early phases of an eruption. In such cases, observatories use remote observations, satellite and ground-based sensors >250 km from the source, to monitor and characterize activity. Remote observational tools played a critical role in a number of recent eruptions, including those at Bogoslof (USA), Kasatochi (USA), Calbuco (Chile), Sarychev Peak (Kuril Islands), Agung (Indonesia), Anak Krakatau (Indonesia), and Chaitén (Chile) volcanoes. During these eruptions, the combination of remote observations (infrasound, lightning, and satellite remote sensing data) enhanced monitoring efforts and eruption characterization (e.g., Coombs et al., 2018; Matoza et al., 2018; Van Eaton et al., 2016).

In this study we retrospectively characterize the VEI 4 eruption of Raikoke volcano, Kuril Islands, on 21–22 June 2019 (Degtyarev and Chibisova, 2019; Firstov et al., 2020; Girina et al., 2019; Rashidov et al.,

* Corresponding author.
E-mail address: kfmckee@carnegiescience.edu (K. McKee).

https://doi.org/10.1016/j.jvolgeores.2021.107354
0377-0273/

2019; Smirnov et al., 2021) to evaluate the state-of-the-art in remote observational tools in application to a closed system volcano. We define "remote" as instruments that are non-local to the volcano which include satellite remote sensors, global lightning networks, and regional and remote infrasound. In a companion paper (McKee et al., this volume), we perform the same evaluation for an open-system volcano, and compare the results of both studies. A volcanic system is considered closed if its conduit lacks pathways for gas escape, which implies no measurable pre-eruptive gas emissions (e.g., Reath et al., 2019a). A recent ground-based survey of gas emissions from active volcanoes in the Kuril Island arc reports no geochemical or emissions data for Raikoke (Taran et al., 2018). Given the long repose (~100 years) since its last major eruption in 1924, it therefore seems likely that Raikoke was a predominantly closed system prior to the 2019 eruption, although a more detailed analysis of TROPOMI SO_2 data collected in 2017–2019 might provide further insight. Using data from remote infrasound and lightning sensors and satellite-borne sensors, combined with plume modeling based on these observations, we estimate eruption onset and cessation times, track *syn*-eruptive variations in infrasonic amplitude and frequency, lightning stroke rate, and plume height, and show pre- to post-eruptive morphology changes.

The Earth science community is working to improve infrastructure to support the reuse of data under the FAIR Data Principles (National Academies of Sciences, Engineering and Medicine, 2020; Stall et al., 2018; Wilkinson et al., 2016). Data are considered FAIR if they are Findable, Accessible, Interoperable, and Reusable. The field of volcanology is multidisciplinary and relies on many data types. This includes volcanic eruption characterization. Given the community-wide efforts towards FAIR data practices, we highlight in the Data and Discussion sections the classification of the data we utilized in this study.

2. Raikoke volcano

Raikoke (48.29°N, 153.25°E, 551 m) is a small (2 × 2.5 km) basaltic stratovolcano in the Kuril Island chain between Japan and Kamchatka (Fig. 1a-b). The Kuril Island chain is part of the Kuril-Kamchatka volcanic arc associated with subduction of the Pacific Plate beneath the Okhotsk microplate. The Kuril volcanoes are sparsely populated but underlie major air traffic routes between Asia, North America, and Europe, making explosive eruptions hazardous to aviation. Raikoke is remote (~1090 km from Sapporo, Japan) and infrequently active (three known historical eruptions) with no local monitoring network and little publicly-available scientific literature. The edifice is unvegetated, with a steep-walled crater measuring 700 m wide and 200 m deep (Gorshkov, 1970). The eastern slope is mantled by lava flows and the southern slope covered by pyroclastic deposits. Known eruptions include a VEI 2 event in 1765 (+/− 5 years) and VEI 4 events in 1778 and 1924 (Gorshkov, 1970; Newhall and Self, 1982). The 1778 eruption prompted the first specifically-volcanological investigation of the Kuril islands (Tatarinov, 1785). The 1924 eruption generated tropospheric aerosol transport resulting in an ice-core signal in Greenland (Holdsworth and Peake, 1985; Lyons et al., 1990; Zielinski, 1995) but no significant aerosol peaks were observed in time series of atmospheric optical extinction (solar intensity; (Sato et al., 1993)). More recently, the Sakhalin Volcanic Eruptions Response Team (SVERT) reported weak fumarolic gas emissions and possible phreatic ash emissions at Raikoke in June 12–13, 2009 that did not lead to a major eruption (McGimsey et al., 2014). This activity coincided with the VEI 4 eruption of Sarychev Peak volcano, ~24 km to the south (Fig. 1b), which began on June 11, 2009 (SVERT, 2009).

3. Data and methods

In our analyses, we utilize primarily infrasound, lightning, and satellite remote sensing (thermal, UV, and visible) data, but we checked additional data types. Table 1 shows the data type that provided information for pre-, *syn*-, and post-eruption periods and the instrument or network, in the case of infrasound and lightning, it came from. Raikoke volcano does not have ground-based instrumentation and the island is too small for the effective use of InSAR techniques. Thermal observations of Raikoke were limited by cloud cover and the closest seismic station from which we were able to obtain data is >20 km away.

3.1. Infrasound

Infrasound is defined as sound below the audible range for humans, 20 Hz (Bedard Jr. and Georges, 2000), with wavelengths ranging from ~20 to 3500 m that can propagate hundreds to thousands of kilometers in the atmosphere (Whitaker and Norris, 2008). Volcano infrasound is a measure of the perturbation of the atmosphere by subaerial/surface volcanic activity (e.g., explosions, gas jetting, lahars, pyroclastic density currents, sub-Plinian to Plinian eruptions) and is recorded at local (<15 km), regional (~15 to 250 km), and remote (>250 km) distances

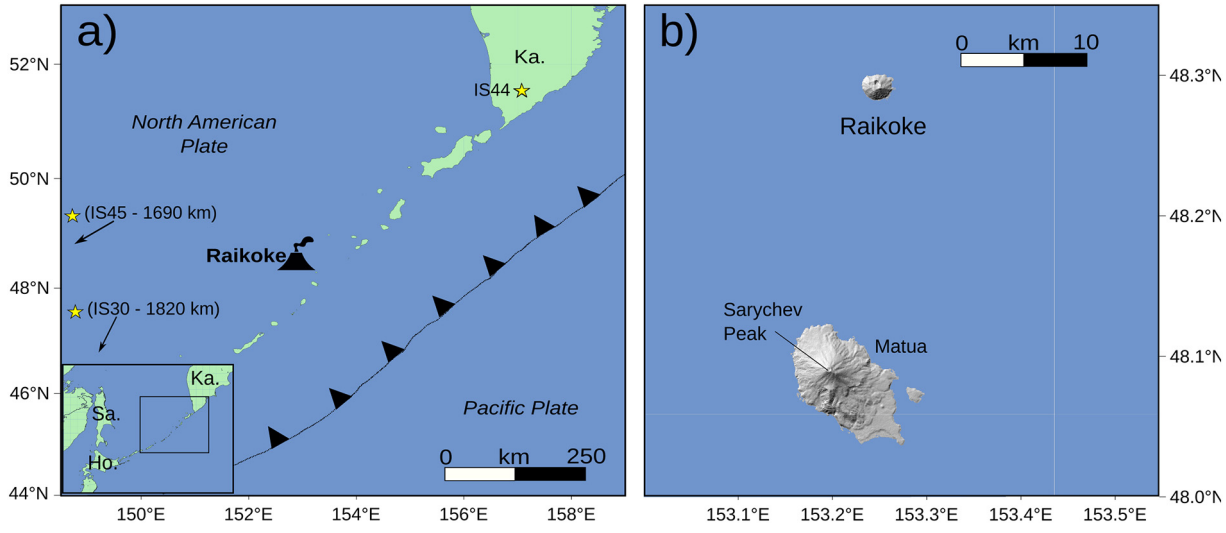

Fig. 1. Location of Raikoke volcano with tectonic context. a) and b) Raikoke volcano, Kuril Islands. Ka = Kamchatka, Sa = Sakhalin, Ho = Hokkaido. Yellow stars = IMS infrasound stations. (For interpretation of the references to color in this figure legend, the reader is referred to the web version of this article.)

Table 1
Data accessibility and analyses.

	Pre-eruption	Syn-eruption	Post-eruption
Utilized	Thermal (**Sentinel-2**), Visible (**Sentinel-2**) time series and satellite imagery	Satellite Detections: Ash (**MODIS**, Himawari), SO2 (**OMI, TROPOMI**); Lightning (GLD360); Infrasound (IMS data); Plume Heights	Modelled Ash Dispersion; Visible Satellite Imagery (**Sentinel-2**); Topography Change (RADARSAT-2)
Inconclusive (checked)	InSAR (ALOS-2); RS Thermal (cloud cover); Seismic at >20 Km distance (**IU PET in IRIS DMC**)	RS Thermal (cloud cover); Seismic at >20 Km distance (**IU PET**)	Seismic at >20 Km distance (**IU PET**)

The columns show the data types and their respective instruments or networks analyzed for each period of the eruption sequence. The rows then highlight whether the data and analyses were utilized or checked, but inconclusive. Bold indicates data can be formally classified as FAIR —Findable, Accessible, Interoperable, Reusable.

from the source (Fee and Matoza, 2013; Matoza et al., 2019). Infrasound detected from a volcano confirms subaerial activity, provides eruption timing (onset and duration) (Fee et al., 2010b, 2013b; Matoza et al., 2011, 2018), and gives a measure of intensity (power per unit area; (Matoza et al., 2013a)) and eruption dynamics (Cannata et al., 2009; Dabrowa et al., 2011; Fee et al., 2010a). Waveform characteristics and signal frequency content relate to the type of activity and variations in eruption (e.g., Fee et al., 2017, 2013a; Johnson et al., 2018; Marchetti et al., 2009; Matoza et al., 2009).

We use data from the infrasound component of the International Monitoring System (IMS), a global network designed for the verification of the Comprehensive Nuclear-Test-Ban-Treaty (CTBT). The infrasound array network has been designed to detect and locate an atmospheric explosion with a yield of at least 1 kt, at any point on the globe, at any time. The network consists of arrays with an average spacing of 1902 km in the Northern hemisphere and 2027 km in the Southern hemisphere. IMS infrasound arrays have an average aperture (largest distance between two sensors composing an array) of two km and consist of four to eight highly sensitive pressure sensors (i.e., microbarometers) that are installed with a wind noise reduction system (Christie and Campus, 2010). The microbarometers sample the pressure field in the vicinity of the sensor at 20 Hz. Infrasound sensors are often deployed as arrays when trying to observe a large region and potential source locations are unknown. The specific IMS arrays used were IS44 (four elements at 621 km), IS45 (four elements at 1700 km), and IS30 (six elements at 1787 km).

We use two different array processing techniques, the Progressive Multi-Channel Correlation (PMCC) (Cansi, 1995) and the Median Cross-Correlation Maxima (MdCCM) (Lee et al., 2013) combined with a weighted least squares estimation of a plane wave arrival (Olson and Szuberla, 2008), to detect and estimate the back-azimuth to signals of interest. Both of these methods give a measure of signal coherency and an estimate of back-azimuth, the notable difference is that PMCC combines the evaluation of coherency with back-azimuth estimation and uses window lengths scaled with frequency, while MdCCM evaluates signal coherency separately from the back-azimuth, which is estimated using the least squares estimation of a plane wave arrival method. We use the PMCC configuration as described in Matoza et al. (2017, 2013b). For the MdCCM detections, we filter the IS44, IS45, and IS30 data from 0.1 to 5 Hz. We use the multitaper method (Riedel and Sidorenko, 1995) for power spectral density estimates on time windows with detections ±10 degrees back-azimuth to the volcano.

3.2. Lightning

Volcanic lightning is a relatively new data type being applied to volcanic eruption monitoring and characterization. Lightning is a transient high-current transfer of charge between oppositely charged regions (Dwyer and Uman, 2014). Lightning emits radiation across a wide range of frequencies, from very low (VLF, 3–30 kHz detectable at <4000 km) to very high (VHF, 30–300 MHz detectable to ~200 km) (Behnke and McNutt, 2014). VLF lightning generated by volcanic eruptions can be detected with global lightning detection networks such as the Global Lightning Dataset (GLD360, operated by Vaisala Inc.),which record the time, location, and strength of individual lightning strokes.

Multiple processes generate charge within eruption columns and clouds, including fracto-emission (fragmentation of solidified magma into ash which releases charge into the plume; James et al. (2008, 2000)) and triboelectrification (the transfer of charge between ash particles when they interact; (Forward et al., 2009; Houghton et al., 2013a; Méndez Harper and Dufek, 2016; Williams et al., 2009)). Fracto-emission and triboelectrification are thought to be the dominant charging mechanisms in the eruption column where air temperatures remain above freezing (James et al., 2008), but as an eruption cloud gains in altitude, the generation of ice and graupel (at temperatures <-20 °C) also facilitate non-inductive ice charging, similar to that found in meteorological thunderstorms (Arason et al., 2011; Prata et al., 2020; Van Eaton et al., 2020).

Previous volcanic lightning studies at Eyjafjallajokull (Aplin et al., 2014; Arason et al., 2011; Behnke et al., 2014; Woodhouse and Behnke, 2014), Redoubt (Behnke et al., 2013; Genareau et al., 2019; Hoblitt, 1994), Sakurajima (Aizawa et al., 2010; Cimarelli et al., 2016; Miura et al., 2002; Smith et al., 2018a), Bogoslof (Haney et al., 2018; Smith et al., 2018b; Van Eaton et al., 2020), Kelud (Hargie et al., 2019), and Calbuco (Van Eaton et al., 2016) observe ash coincident with electrical activity and lightning generation. These observations suggest volcanic lightning may be a valuable, early indicator of an explosive, ash-bearing eruption, particularly for remote volcanoes lacking dedicated monitoring instruments or in regions where meteorological lightning is rare, such as high latitudes (McNutt and Williams, 2010).

For this analysis we use globally detected lightning strokes from the GLD360. Our dataset includes strokes within a 300 km radius of Raikoke. We use a large radius to account for the drifting and eastward elongation of the eruption cloud due to the wind field. We cleaned the GLD360 dataset of meteorological lightning strokes by visual inspection of the lightning times and locations with respect to satellite imagery. The GLD360 data is composed of date, time (to the nearest millisecond), latitude, longitude, polarity, and estimated peak current (kA) for each recorded stroke. In total there were 753 volcanic lightning strokes included in this analysis.

3.3. Satellite remote sensing

Satellite remote sensing data are used to characterize various aspects of the Raikoke eruption. These data are particularly useful in the absence of local, ground-based instrumentation. We focus on the three primary types of satellite volcanic monitoring techniques to make these characterizations: degassing, visible/thermal, and deformation (Poland et al., 2020).

Instruments designed to measure atmospheric SO_2 provide a way to remotely monitor volcanic SO_2 flux. The Ozone Monitoring Instrument (OMI) (e.g., Carn et al., 2017, 2016) and TROPOspheric Monitoring Instrument (TROPOMI) (Veefkind et al., 2012) instruments are sensitive to the absorption features of SO_2 in the ultraviolet (UV) wavelengths. TROPOMI was launched in 2017 and provides the highest spatial resolution achieved by a UV satellite sensor to date (~3.5 × 5.6 km at nadir; (Theys et al., 2019, 2017)). OMI has lower spatial resolution

(~13 × 24 km at nadir), but it has been operational since September 2004 and has generated the longest, continuous satellite-based record of volcanic SO_2 emissions (Carn et al., 2017, 2016). These instruments are sensitive enough to monitor both active degassing occurring during eruptions (Carn et al., 2016) and passive degassing occuring before and after eruptions above detection limits (Carn et al., 2017).

Optical remote sensing images in the visible and thermal infrared wavelengths (Asrar, 1989), can provide information about the reflected and emitted energy from the surface of the earth. Visible Near Infrared (VNIR) and Short Wave Infrared (SWIR) sensors primarily detect reflectance and have smaller pixel sizes than their thermal counterparts, are available on a great number of instruments (e.g., ASTER, Landsat, Sentinel-2) and are effective at identifying healthy vegetation (e.g., Carlson and Ripley, 1997). We use these data to identify changes in the shape and size of the volcanic edifice, the emplacement of volcanic deposits, and effects of the eruption on surrounding vegetation.

Thermal data, acquired in the Thermal Infrared (TIR) wavelengths, detect radiant energy emitted from the surface, from which surface temperature can be derived using Planck's law (Gillespie et al., 1998). By examining how surface temperature changes over time, using multiple satellite acquisitions, it is possible to identify pre-eruptive changes in thermal output that could suggest changes within the system, co-eruptive changes corresponding to the location of active flows, and post-eruptive changes that could help to identify the likelihood of a subsequent eruption. In this study we use the Advanced Spaceborne Thermal Emission and Reflection Radiometer (ASTER) sensor to make these measurements (Reath et al., 2019b) due to its accuracy and high spatial resolution.

3.3.1. SAR and InSAR

Synthetic aperture radar (SAR) satellites emit pulses of microwave energy and measure reflectance from the Earth's surface. The amplitude and coherence of the returned signal can be used to map changes in surface morphology and reflectance, permitting the mapping of lava flows and other volcanological processes (e.g., Dietterich et al., 2012; Lu et al., 2004; Arnold et al., 2018; Di Traglia et al., 2018; Pallister et al., 2013; Wadge et al., 2012). In this study, by comparing RADARSAT-2 SAR amplitude data acquired before and after the Raikoke eruption we are able to map changes in vent dimensions. This approach is limited chiefly by the oblique look angle of the satellite (angle between the satellite and the ground surface), which makes interpreting changes in horizontal dimensions nonunique. We also investigated InSAR (interferometric SAR) techniques, which directly interfere two SAR images acquired at approximately the same location but at different times in order to detect centimeter-level changes in surface elevation along the line-of-sight between the satellite and surface (e.g., Hooper et al., 2004; Pritchard and Simons, 2004). InSAR can be a powerful remote sensing tool for detecting ground deformation caused by magmatic and other processes, but we find that it is not well suited for the Raikoke eruption due to the small size of the island.

3.3.2. MODIS and Himawari

The Moderate Resolution Imaging Spectroradiometer (MODIS) launched on both the Terra (1999) and Aqua (2002) satellites provides 1 km resolution thermal data with an acquisition rate of 4 per day. These data are utilized to detect volcanic thermal anomalies associated with eruptions (e.g., Coppola et al., 2016; Wright et al., 2004). Thermal data are also obtained from the geostationary weather satellite Himawari-8, operated by the Japanese Meteorological Agency, which has a multispectral imager onboard that images Asia and the Pacific regions every 15 min with a 4 km^2 pixel size (Bessho et al., 2016).

We use MODIS and Himawari-8 data primarily to establish the brightness temperature at a wavelength of 11 μm (BT11; band 13 for Himawari-8 and band 31 for MODIS) of the ash plume. This is considered to be equivalent to the atmospheric temperature at the top of the plume (Corradini et al., 2018; Oppenheimer, 1998; Prata and Grant, 2001). The coldest pixel in a grid over the volcano, that is defined as spanning between longitudes of 153.1 and 153.59 and latitudes of 48.09 and 48.53, is used to estimate the maximum plume height. We characterize the uncertainty related to this coldest pixel value by considering an error of $+ -$ 2 K as in Corradini et al. (2018). We then use European Centre for Medium-Range Weather Forecasts *Re*-Analysis-Interim (ERA-Interim) data to identify the corresponding atmospheric height at which this temperature is reached (Berrisford et al., 2011; Dee et al., 2011). This procedure allows for a maximum plume height, and an associated uncertainty, to be determined for each satellite image acquisition. MODIS data are used to determine the average temperature of the plume from the Raikoke eruption from three separate points in time acquired during the Plinian phase, and Himawari-8 data are used to determine the average temperature of the plume over 24 h and create a time series.

3.3.3. Sentinel-2

The VNIR and SWIR data were acquired by the Sentinel-2 sensor. This sensor provided the best high spatial resolution (10 m VNIR band, 20 m SWIR bands) coverage in these wavelengths due to its high revisit time (5 days at the equator) (Drusch et al., 2012). The high spatial resolution of the data provided a means to identify changes in surface area that occurred during the eruption by comparing images acquired before and after. VNIR images have the benefit of highlighting the presence of vegetation, providing a quick solution to identifying vegetation killed as a result of a new flow or covered from ash fall. The Normalized Difference Vegetation Index (NDVI) compares reflectance values at different VNIR wavelengths and provides a measure of vegetative health, with higher values corresponding to healthier vegetation (Carlson and Ripley, 1997). NDVI has the added benefit of identifying some vegetation that may have been missed by a simple VNIR RGB image. We apply NDVI to Sentinel-2 data to observe post-eruptive algae blooms. Volcanic eruptions can trigger algal blooms where diffuse iron from volcanic ash interacts with water and fertilizes existing algae (e.g., (Armon and Starosvetsky, 2015; Kim et al., 2020; van Stokkom, 2013). All Sentinel-2 data we use in this study are openly available at the Sentinel-hub EO Browser (https://www.sentinel-hub.com/explore/eobrowser).

3.3.4. Ultraviolet (UV) remote sensing

Several operational UV satellite instruments provide measurements of total column SO_2 in volcanic plumes, with variable sensitivity due to differences in spatial and spectral resolution (Carn et al., 2016). Here, we use SO_2 data from TROPOMI on the European Space Agency (ESA) Sentinel-5 Precursor (S5P) satellite and OMI on NASA's Aura satellite. To investigate SO_2 emissions prior to and during eruption, we use the operational TROPOMI and OMI SO_2 products (Li et al., 2017; Theys et al., 2017). Unless otherwise noted, the UV SO_2 retrievals reported here assume a lower stratospheric (STL; ~17 km altitude) plume altitude appropriate for the Raikoke eruption; above altitudes of ~5 km the UV SO_2 retrievals and derived SO_2 mass are relatively insensitive to the actual plume altitude. TROPOMI SO_2 products used here (S5P_OFFL_L2__SO2) are publicly available from the Copernicus Sentinel-5P Pre-Operations Data Hub (https://s5phub.copernicus.eu/dhus/#/home). OMI SO_2 products (OMSO2_003) are publicly available from the NASA Goddard Earth Sciences (GES) Data and Information Services Center (DISC; https://disc.gsfc.nasa.gov/datasets/OMSO2_003/summary).

In this study we use the satellite SO_2 data to gain insight into eruption intensity and magnitude, and to identify potential eruption precursors manifested in SO_2 emissions. Raikoke is absent from the OMI-derived SO_2 emissions database (Carn et al., 2017), indicating either that it was a closed system prior to the June 2019 eruption (at least with respect to SO_2 emissions; note that this does not preclude degassing of other volatile species such as CO_2) or that any SO_2 emissions in 2005–2018 were below satellite detection limits (which is

~30 tons/day on an annual average basis). We use the TROPOMI SO_2 data to investigate SO_2 degassing on shorter timescales prior to and during the 2019 eruption. Although the eruption generated a stratospheric SO_2 cloud that persisted in the atmosphere for some time, a detailed analysis of the long-range transport and lifetime of the volcanic cloud is beyond the scope of this paper.

3.4. Plume modeling

The sustained volcanic plume produced by the Raikoke eruption is investigated with the one-dimensional plume model of Degruyter and Bonadonna (2012). Such models are based on buoyant plume theory (Morton et al., 1956) and solve the conservation of mass, momentum, and energy equations to determine the dynamics and characteristics of a plume. It is assumed that the plume is in steady state, in two respects: (1) changes in plume characteristics such as mass eruption rate (MER) occur over time scales much longer than the travel time from the vent to the plume top; and (2) the plume rise timescale is longer than the turbulence timescale and therefore turbulent velocity fluctuations do not need to be described explicitly. Instead, the rate of turbulent entrainment of ambient air into the plume is assumed to be a constant fraction of the average upward velocity of the plume (the radial entrainment coefficient) (Morton et al., 1956). In the presence of a crosswind, additional entrainment is assumed to occur at a rate that is proportional to the crosswind velocity (the wind entrainment coefficient)(Bursik, 2001; Devenish et al., 2010; Hoult and Weil, 1972). The total entrainment rate is the sum of the radial and wind entrainment. Although the model is simple, it takes into account effects of different processes such as wind, particle fallout, humidity, and phase changes of H_2O (Bursik, 2001; Glaze et al., 1997; Mastin, 2007; Woods, 1993). Real atmospheric conditions can also be incorporated.

A Monte Carlo setup is used to determine the MER time-series for the Raikoke eruption as the initial source conditions (velocity, gas mass fraction, magma temperature, plume radius) are unknown. These are sampled randomly from uniform probability distributions. The parameter ranges that were explored can be found in Sup. Table 1. The explored ranges are large as little is known about the source conditions of this eruption. We keep the entrainment coefficients in the model (wind and radial) and the meteorological data used for the atmospheric conditions constant. The values of the radial and wind entrainment coefficients are 0.1 and 0.5, respectively as in Degruyter and Bonadonna (2012). Atmospheric inputs include temperature, humidity, and wind vectors as a function of height in the atmosphere. To account for uncertainty in using meteorological data from different sources, we explored the use of meteorological data from the closest radiosonde and ERA-Interim data. As we did not find a significant difference between the different weather datasets, we used only the ERA-Interim data as the atmospheric conditions in the Monte Carlo plume modeling. For each height measurement in the time-series, a Monte Carlo simulation composed of 500 runs is performed. The Monte Carlo simulations are constrained with the observed plume heights. To account for bending of the plume due to wind we follow the procedure of Mastin (2014) and, for each set of input parameters, run the simulations both accounting for and neglecting the effect of wind. In the former case, the top plume height is taken as the sum of the height of the center line and the plume radius. The minimum top modelled plume height from both of these runs is then chosen to compare with the observed top plume height. For each run in the Monte Carlo simulation the modelled plume height is compared to the observed plume height (determined by the Himawari BT11 measurement as described in Section 3.3.1). If the modelled plume height is within error of the observed plume height (i.e., between the minimum and maximum, or average if maximum is not available, plume heights calculated as $+-2$ K for the picked coldest pixel in the satellite image), we consider the simulation as a match and record the initial MER. When multiple modelled plume heights match the observations, the range of MERs at each time is recorded. The average, minimum and maximum are taken from this range and are presented in the results section. We also examine the modelled plume temperature profiles from the matched model simulations to examine if undercooling of the plume has occurred.

4. Results and observations

4.1. Infrasound

We detect the Raikoke eruption with IMS arrays IS44, IS45, and IS30 with IS44 detections being the most comprehensive. We observe six pulses lasting 13–43 min with interpulse times from 13 to 33 min. Fig. 2a shows the best beamform of the IS44 array data. The first pulse starts on 21 June 2019 at 17:50 UTC and the main Plinian phase begins on 21 June at 22:29 UTC and lasts 3.5 h (Fig. 2a–b). In Fig. 2b, we plot the peak frequency through time over the spectrogram. The peak frequency is consistent from pulse to pulse, but during the Plinian phase the peak frequency decreases from ~0.2 Hz to ~0.1 Hz and remains there for the duration of the eruption. Fig. 2c shows the spectra of several time periods where the color of the curve matches the color of the detection dots in Fig. 2a. Again we observe this decrease in peak frequency between the pulses and the Plinian phase. A photo was captured of the beginning of the Plinian phase from the International Space Station (ISS) (Fig. 2d). We can distinguish the six pulses with both IS44 and IS45 data, but not IS30 data (Figs. S1–S6).

4.2. Lightning

The initial lightning stroke occured on 21 June at 17:48:21.645 UTC (Fig. 3). The lightning continued for over 16 h until the final stroke on 22-June at 09:53:54.045 UTC. We observe peak stroke rates from 21 June 22:28 to 22 June 02:34 UTC with rates reaching >20 strokes per 5 min (Fig. 4a). The peak current measured for a single stroke during this eruption was +104.9 kA (Fig. 4b) and the highest estimated peak current strokes are closest to the vent (Fig. 3). The majority of the strokes were positive in-cloud strokes (as defined by being <15 kA). In Fig. 3a–f, we note that the strokes are above/slightly NW of Raikoke, while in Fig. 3g–i the strokes also extend to the east.

4.3. Satellite remote sensing

Several different sensors observing the VNIR, SWIR, and TIR wavelengths provided valuable information for this study. In an attempt to identify pre-eruptive unrest, we analyzed high spatial resolution (i.e., ASTER) TIR data before the eruption and were unsuccessful due to cloudy weather conditions and a lack of regular acquisitions. The vast majority of acquisitions were obscured by clouds, and the first partially clear observation before the eruption, made on 2 December 2018, revealed no obvious volcanic thermal features.

We determined the height and position of the dispersing ash plume from MODIS and Himawari data. A series of short distinctive pulses can be seen in the height time series data shown in Figs. 3 and 4c, with the first pulse detected at 18:10 UTC. A more sustained eruption pulse starts at 22:40 and lasts until 2:00 where the plume height decreases. We observe a maximum eruption plume height of 11 km a.s.l. at 23:40. This is followed by two additional pulses. During the sustained pulse, a number of measurements had temperatures colder than the surrounding atmosphere, suggesting undercooling. The same is observed with the MODIS data at 22:45 and is further suggested by the flat top of the plume seen in the NASA ISS image (Fig. 2d).

Cloud-free TIR data were not available soon enough after the eruption to track cooling flows. We used Sentinel-2 VNIR data to identify a ~14% increase in surface area that occurred during the eruption (Fig. 5) and a *syn*-eruptive expansion of the crater was identified and confirmed with SAR amplitude imagery (Fig. 6). Figs. 5 and 6 show new deltas to the northeast, south, and southwest part of the island

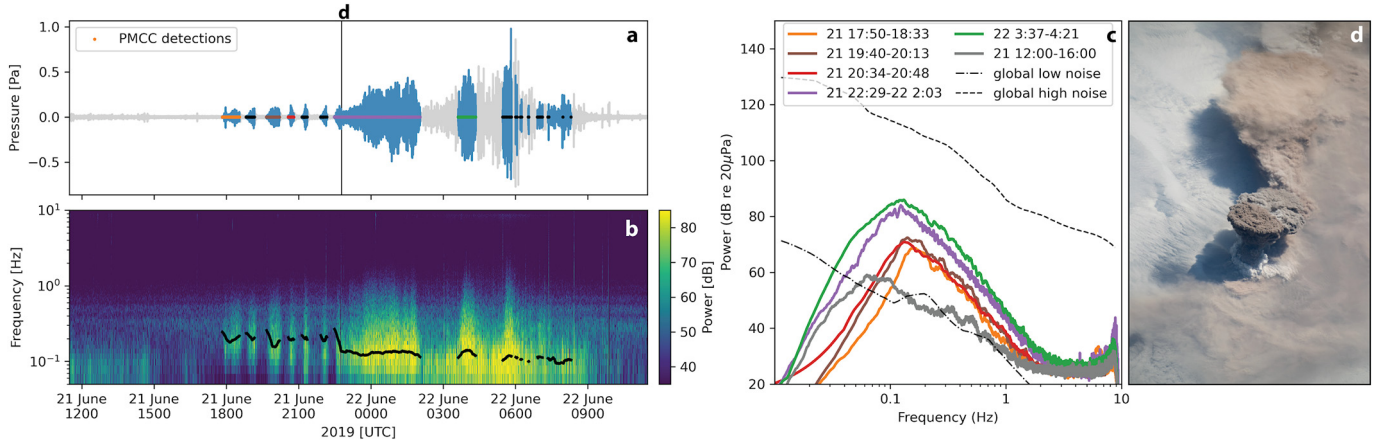

Fig. 2. Raikoke Eruption Infrasound a) Beamformed waveform from IS44 array with PMCC detections plotted as red, black, green, blue, light purple, and orange bars, b) Spectrogram with the peak frequency through time highlighted by the black line, c) Spectral curves for specific windows of the eruption. Color of the spectral curve corresponds to the color of PMCC detections in a. The gray curve is the noise from 21 June 12:00 to 16:00. The dashed curves are the International Data Centre (IDC) infrasound global low and high noise models for IMS infrasound arrays (Brown et al., 2014). d) Photograph from the International Space Station captured on 6/21/2019 at 22:45:53 at the start of the Plinian phase. (For interpretation of the references to color in this figure legend, the reader is referred to the web version of this article.)

likely from pyroclastic density current (PDC) deposits; PDCs are visible in the ISS photo (Fig. 2d). We applied an NDVI equation to these data which revealed characteristics of healthy vegetation in the water to the south of the island. This is likely an algae bloom that developed as a result of eruptive ash altering ocean chemistry (e.g., Genin et al., 1995; Lindenthal et al., 2013; Mantas et al., 2011) (Fig. 7). This bloom persisted for 2 months after the eruption.

We inspected TROPOMI SO_2 data covering Raikoke on June 15–20, 2019, prior to the eruption, but found no evidence for pre-eruptive SO_2 emissions detectable from space. OMI measurements since 2005 also show no evidence for detectable SO_2 emissions from Raikoke (Carn et al., 2017).

A TROPOMI overpass at ~02:20 UTC on June 22, about 6 h after the onset of the Raikoke eruption, showed high SO_2 amounts (~0.3 Tg SO_2) in a cloud extending ENE from the volcano (Fig. 8), consistent with the prevailing upper tropospheric winds. The highest SO_2 column amounts were measured in the proximal region of the cloud generated by the main Plinian phase of the eruption, which was ongoing at the time of the overpass (based on high lightning stroke rates). The TROPOMI data indicate that lesser amounts of SO_2 were emitted during the earlier phase of the eruption. Based on data from TROPOMI and other UV and IR sensors, the peak SO_2 mass loading of ~1.4 Tg SO_2 was not measured in the Raikoke eruption cloud until June 23–24 (e.g., de Leeuw et al., 2020), suggesting that high volcanic ash loading in the fresh eruption cloud on June 21–22 compromised the SO_2 retrievals. The SO_2 cloud remained detectable by TROPOMI and other satellite sensors until late August 2019, indicating significant stratospheric SO_2 injection.

4.4. Plume modeling

We used buoyant plume modeling to estimate the MER for the Raikoke eruption. In Fig. 4c we show the average MER estimates for each determined plume height during the eruption in black. The associated error bars signify the minimum and maximum MER estimates. From the maximum plume height we found a maximum MER of 1.62 $\times 10^6$ kg/s. The MERs for the observed six pulses before the peak of the eruption were calculated with an average value of 9.1 $\times 10^5$ kg/s and a range of 0.33–1.46 $\times 10^6$ kg/s. Based on this MER time series, we estimate the total erupted mass as ranging between 2.87 and 6.72 $\times 10^{11}$ kg, with an average value of 4.39 $\times 10^{11}$ kg.

5. Discussion

Our observations of the 2019 Raikoke eruption indicate three distinct eruption phases: waxing-pulsatory, main Plinian, and waning (Fig. 4).

5.1. Waxing-pulsatory phase

The waxing-pulsatory phase starts on 21 June at 17:50 UTC with six pulses, which are well documented by temporally-aligned infrasound, lightning, and ash plume Himawari data (Fig. 4). We suggest this is the latest possible eruption onset time as there may have been lower intensity activity that started earlier and was below detection limits. However, Firstov et al. (2020) examined infrasound data from local instruments and noted a similar onset time. These pulses have similar infrasonic intensity, lightning stroke rates, and plume heights. We interpret these pulses as 'throat-clearing', Vulcanian to Plinian explosions given their duration and the ash-rich plumes. The occurrence of lightning coincident with these pulses suggests the presence of juvenile material (Smith et al., 2018a). There is a clear increase and decrease in the lightning stroke rate for each pulse as the eruption starts, strengthens, and then stops (as indicated by infrasound, plume height, and MER (Fig. 4)). The lightning stroke times and the infrasound detections occur within seconds or minutes of each other, and there are clear pauses between the lightning related to the smaller eruptive pulses. This may indicate that charging for the smaller, initial events is related to active eruptive processes (electrostatic charging of the ash particles in conjunction with turbulence in the plume separating the charge).

5.2. Main Plinian phase

The main Plinian phase began on 21 June at 22:29 UTC, lasts ~3.5 h, and is marked by infrasound signal amplitude increase and peak frequency decrease, high lightning stroke rate, and increasing ash plume heights. The infrasound signal indicates an hours-long, sustained eruption and the lightning and plume observations indicate a multiphase mixture that formed a buoyant vertical column. While these observations align with the description of Plinian (Cioni et al., 2015), specific classification of each phase of the eruption requires analysis of the deposits (Pyle, 1989; Walker, 1973). Similar drops in peak frequency have been observed during the 2006 eruption of Tungurahua volcano, Ecuador in the transition from sub-Plinian to Plinian (Matoza et al.,

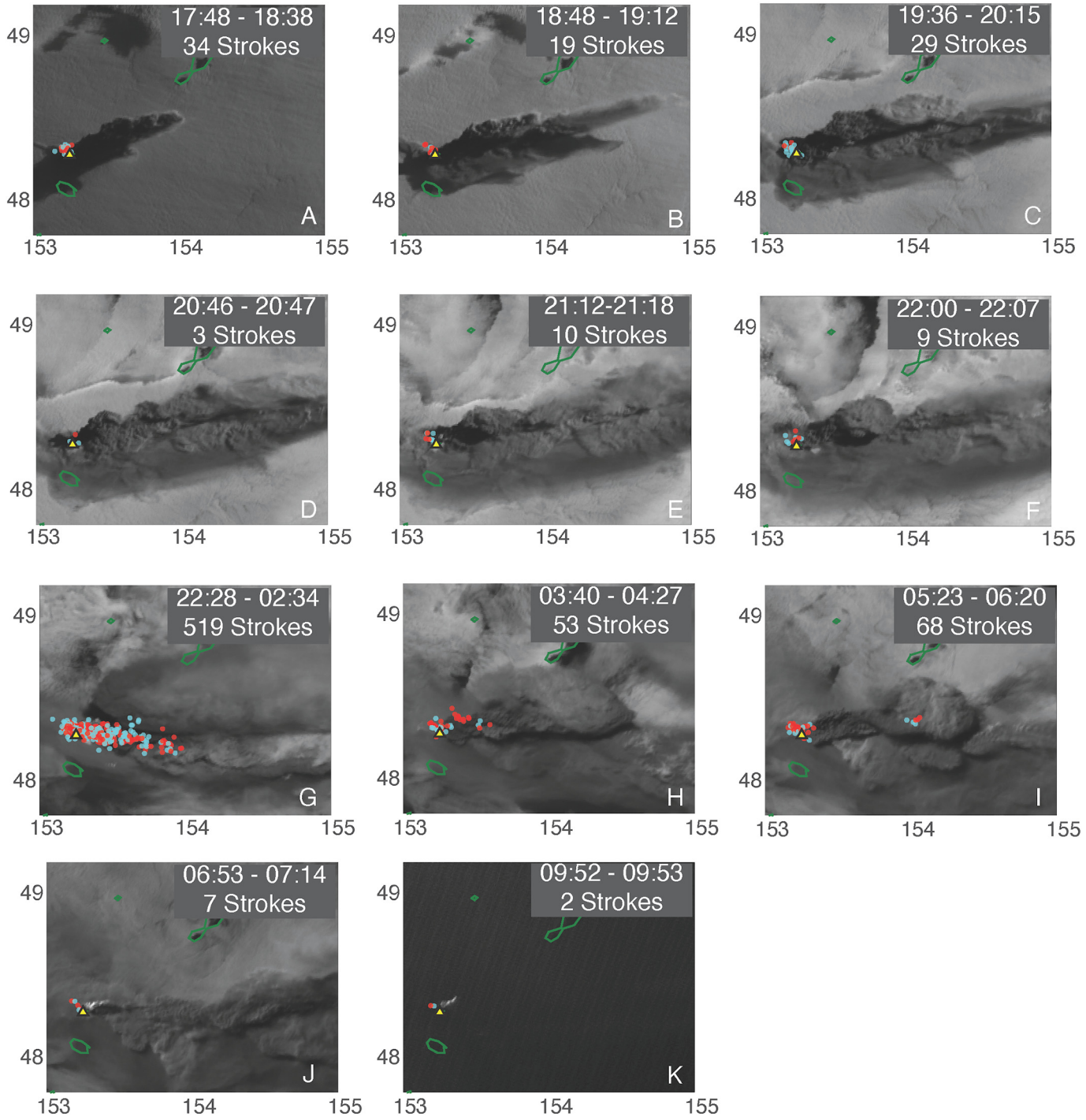

Fig. 3. Raikoke eruption satellite observations through time overlaid with lightning locations (colored circles). Visible light satellite images from Himawari. Red is positive, blue is negative, the yellow triangle shows the volcano location, and green outlines are the surrounding islands. The first six pulses (A-F) were small impulsive events with low levels of lightning. The 7th event (G) was the largest and formed a plume to 13 km, and had several hundred lightning strokes. Strong winds affected all plumes.

2009). This phase was also observed visually by the ISS (Fig. 2d) and produced detectable thermal and SO_2 anomalies. The migration of the lightning strokes and the plume are consistent with wind shearing. The correlation between the MER and the plume height time series is strong due to no significant variation in the weather conditions above the island.

The flat appearance of the top of the ash plume of Raikoke, seen by the ISS (Fig. 2d), is a distinguishing feature of the eruption column. A potential explanation for this phenomenon is undercooling of the plume, which occurs when the top of the plume is colder than the surrounding atmosphere (Woods and Self, 1992). This can occur when momentum causes a plume to overshoot the level of neutral buoyancy. In a stratified atmosphere, the overshoot can bring the cold air and ash plume mixture to the warmer stratosphere. Adiabatic cooling can make the top of the plume colder. These phenomena have been observed at many eruptions such as Mount St Helens (1980), Mount Pinatubo (1991), and El Chichón (1982) (Holasek et al., 1996; Holasek and Self, 1995). The colder portion of the plume is denser and can sink to give the flat top

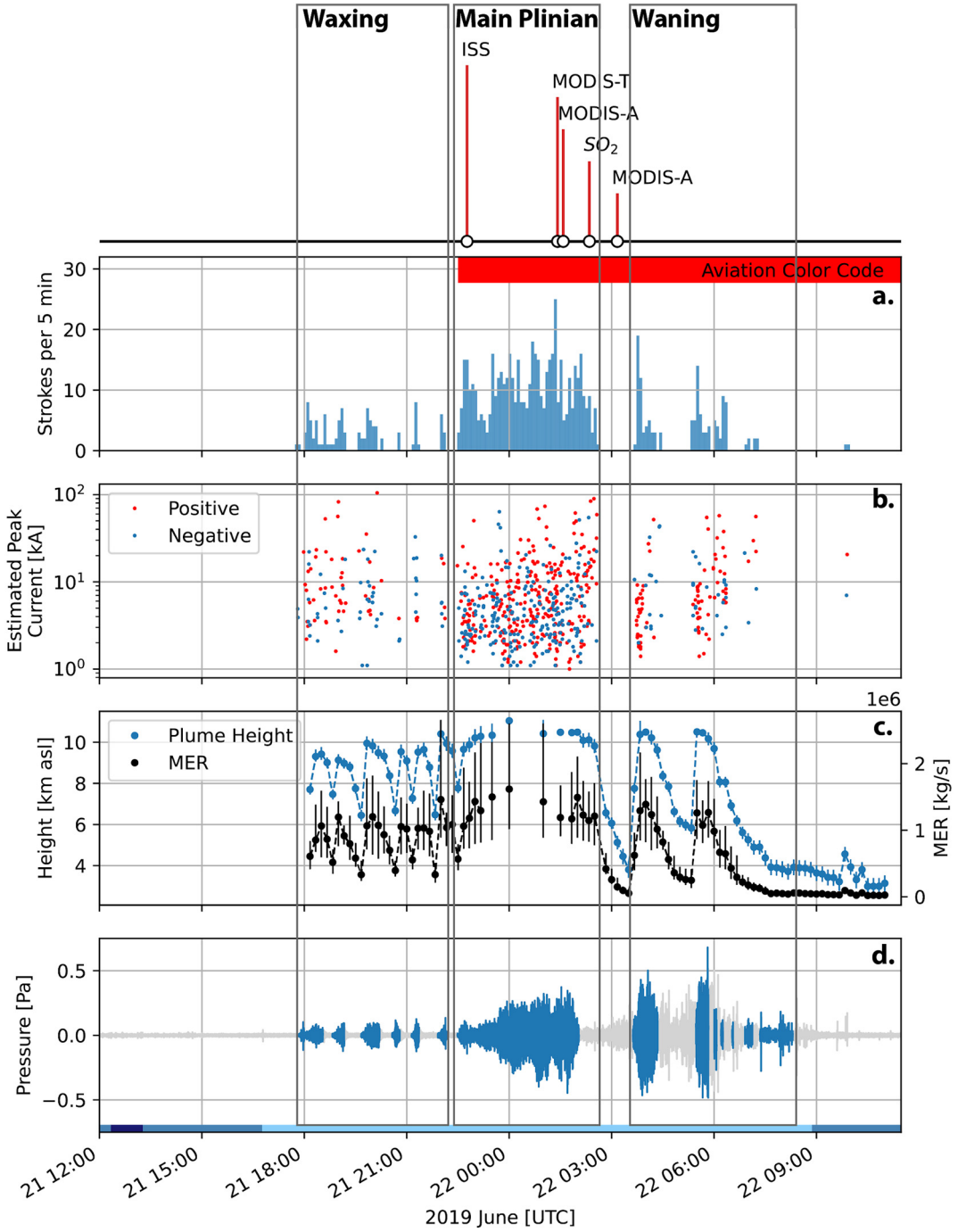

Fig. 4. Comparison of lightning, plume height, mass eruption rate (MER) and infrasound at Raikoke. a) Lightning strokes per 5 min, b) Estimated peak current per stroke (red is positive; blue is negative), c) Plume height above sea level (10 min increments) in blue and MER in black estimated from plume height with vertical lines showing error, d) Beamformed infrasound trace with times of coherent detections plotted in blue. Infrasound data are filtered from 0.1 to 5 Hz. (For interpretation of the references to color in this figure legend, the reader is referred to the web version of this article.)

appearance of the plume (Woods and Self, 1992). In the case of Raikoke, the ISS image evidence is supplemented by the thermal satellite data. Himawari and MODIS measurements show that some pixels near the centre of the plume are colder than the atmospheric temperature profile. Modeling of the plume temperature profiles with the one-dimensional plume model also indicates that the top of the plume is colder than the surrounding ambient temperature (Sup. Fig. 4). An alternative explanation is that the overshooting plume top was fluctuating and the photo was taken when the top was dropping. 3D plume models frequently show fluctuations in the height of the overshooting top (e.g., Suzuki and Koyaguchi, 2009) so this cannot be discounted.

Furthermore, the uncertainties related to the calculation of the plume heights should be considered. We used the brightness temperature acquired by the Himawari satellite and the atmospheric temperature profile to determine the plume height. For this approach, an assumption has to be made as to whether the plume is above or below the tropopause. If assumed to be below the tropopause (as assumed in this study), the coldest pixel in the satellite image will give the highest plume height. Whereas, if the plume is above the tropopause, the hottest pixel is actually correlated to the highest plume height due to the temperature inversion at the tropopause. In this case, the hottest pixel should be used with the stratospheric temperature profile to calculate

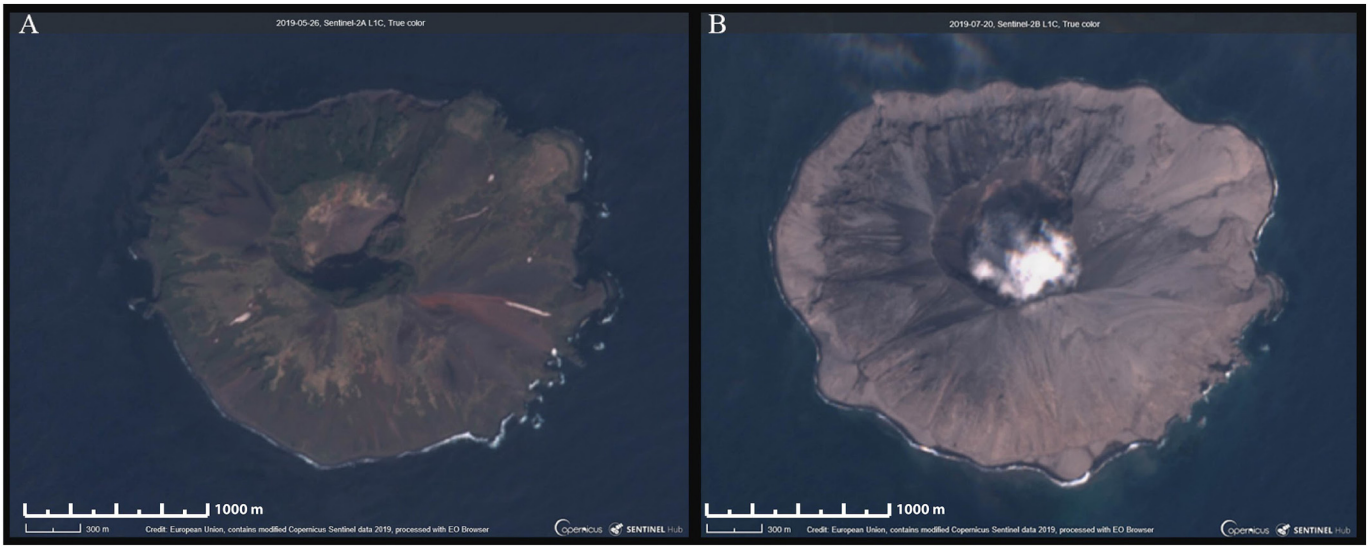

Fig. 5. Post-Eruption Raikoke - Sentinel-2 true color imagery of Raikoke island acquired before (A: 26 May 2019) and after (B: 20 July 2019) the eruption demonstrating both the ~14% increase in surface area of the island and the change in shape of the north section of the crater the occurred during the eruption.

the maximum plume height. This leads to a non-unique solution of the height of a pixel at a given temperature (Schneider and Hoblitt, 2013). Without independent observations of the volcanic plume, it can be difficult to say which approach is suitable for the plume in question,which can lead to large uncertainties in the plume height. As we use the plume height to determine the MER with the plume modeling, it could also lead to large uncertainties in the MER estimates. By looking to see if the brightness temperature at the center of the plume is warmer than the surrounding plume (Schneider and Hoblitt, 2013), we estimate that the plume could have reached into the stratosphere at 00:10, 01:30, 01:40, 03:50, 04:00 and 05:40 UTC (Fig. S8). Although this approach is uncertain, an independent observation would be required to accurately determine if the plume reached the stratosphere. Based on the highest brightness temperatures at these times, the plume could have reached heights as high as 29 km a.s.l. - much higher than the heights determined in Fig. 4c where we assumed the plume was at the tropopause. As a

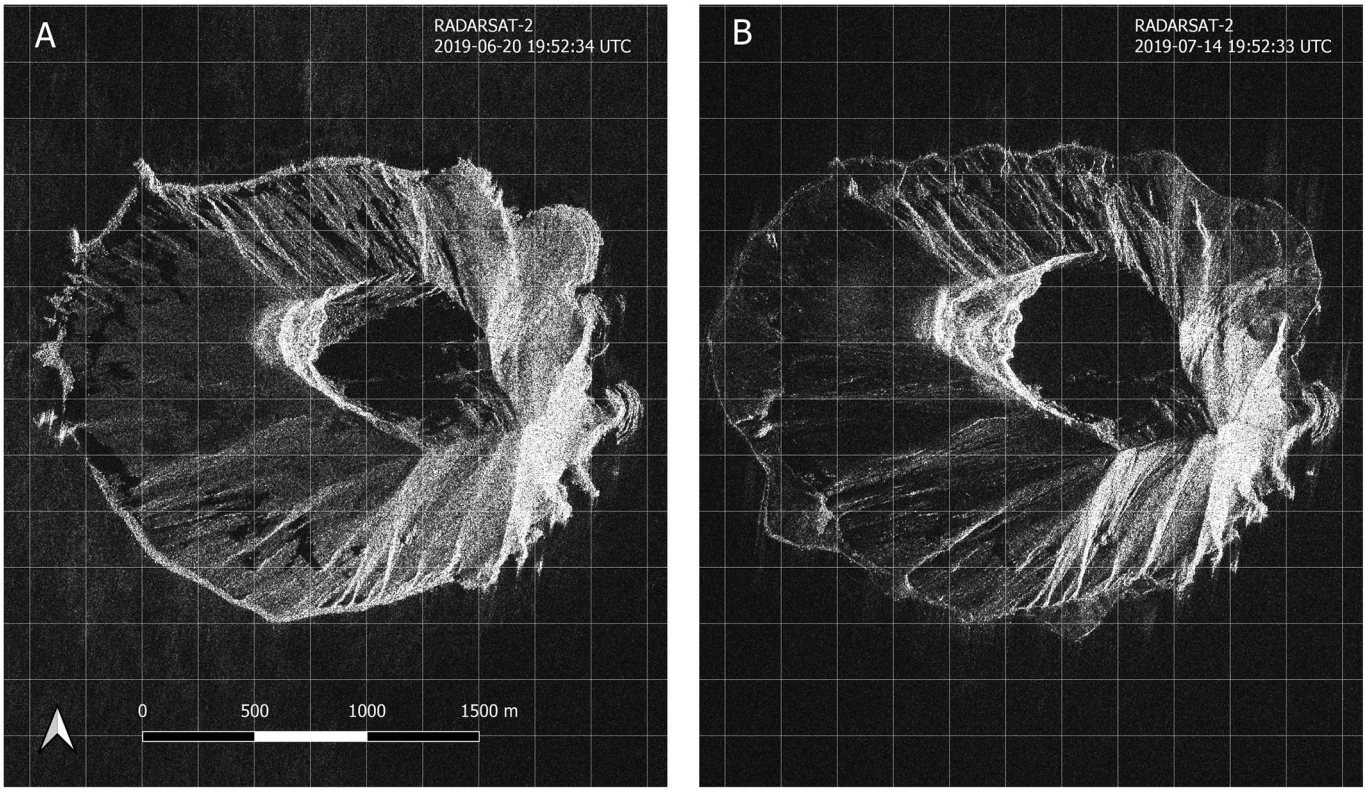

Fig. 6. Post-Eruption Crater morphology of Raikoke - Descending-mode RADARSAT-2 amplitude imagery shows changes in island morphology. A) Pre-eruptive image from 20 June 2019, and B) post-eruptive image from 14 July 2019. Grid spacing is 250 m. Due to the look angle of the satellite there are distortions and the bottom of the crater is shadowed, but it is evident that the crater has expanded to the north about 100 m. The crater has also expanded to the west, but this is difficult to quantify due to distortion introduced by the satellite look angle.

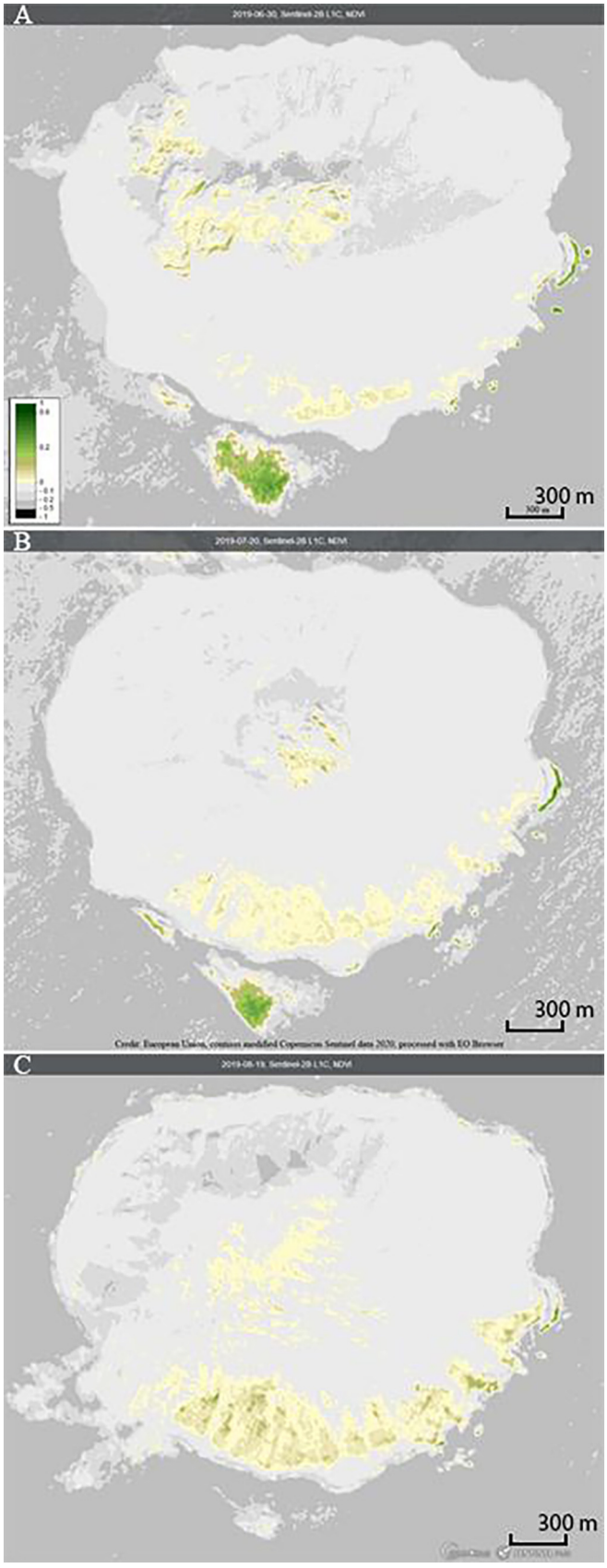

Fig. 7. Post-Eruption Raikoke - NDVI imagery demonstrating the presence and health of vegetation as a result of an algae bloom to the south of Raikoke Island that appears after the eruption (A: 30 June 2019) and subsequently disappears (B: 20 July 2019, C: 18 August 2019).

result, it is vital to be aware of this limitation and acknowledge the potentially large uncertainties in the estimated plume heights.

In the main Plinian phase, we observe the highest lightning stroke rates and plume heights, which suggest ice-charging as an additional lightning generation mechanism (Arason et al., 2011; Prata et al., 2020; Van Eaton et al., 2020). Van Eaton et al. (2020) show that lightning generation is amplified when a plume exceeds the −20 °C isotherm. This temperature coincides with ~7.5 km asl according to ERA-Interim temperature profiles. Looking at the plume heights (Fig. 4 panel c), we can see that each plume pulse reaches this height. This indicates, in addition to electrostatic charging mechanisms, that ice charging is likely playing a role in lightning generation. This is especially likely for the extended 7th infrasonic pulse, when the lightning occurred at the farthest distance (~65 km) from the vent, downwind with the plume. Assuming that the majority of pyroclastic material would have fallen out at this distance, it is likely that the lightning generation in the far plume is related to increased ice-charging. This eruption gives insight into volcanic lightning development. Overall, it can be determined that the rates of volcanic lightning correlate with increases in plume height and MER.

5.3. Waning phase and post-eruptive phenomena

The main Plinian phase is followed by a waning phase with two pulses that have decreasing lightning stroke rates and plume heights. Given the plume heights and durations, these pulses are classified as Vulcanian to Plinian in scale (Houghton et al., 2013b; Pyle, 2015, 1989; Walker, 1973). The eruption fell below detection limits for infrasound, lightning, and ash plume detections on 22 June at about 8:15 UTC, but activity may have continued at lower levels past this time. The SO_2 drifted to the ENE and was observable into August 2019. The ash paralleled the SO_2 moving to the E and was detectable 2 days beyond the start of the eruption in MODIS images.

Analysis of post-eruption imagery is a powerful tool for understanding eruption dynamics and impacts and for preparing for future eruptions. Following the end of the eruption, we were able to resolve the change in island size and shape as well as the increase in crater area. We also document a likely eruption-induced algal bloom.

5.4. State-of-the-art and limitations in remote characterization of volcanic activity

This study demonstrates the utility of multi-parameter remote sensing efforts to document a precise timeline for a remote eruption, and to characterize *syn*-eruptive processes. We did not detect pre-eruption deformation, outgassing, or thermal anomalies. The lack of outgassing and thermal detections is consistent with what is anticipated for a closed system (Chaussard et al., 2013; Reath et al., 2019a). The lack of detected deformation may be due to the small footprint of the island, which generally limits effective use of InSAR techniques, or because the island did not deform significantly prior to eruption.

The eruption detection time (21 June at about 17:50 UTC) is well resolved with consistent infrasound, lightning, and Himawari ash plume detections. We suggest this is the latest possible eruption onset time as there may have been lower intensity activity that started earlier and was below detection limits. The waxing-pulsatory and main Plinian phases are well-documented by temporally-correlated lightning, infrasound, and ash plume detections. The waning phase is less well-constrained by infrasound data as the wind noise increased at the closest recording station (IS44). The high temporal resolution (1 image every 10 min) of the Himawari TIR dataset facilitated the comparison between ash plume heights and the lightning and infrasound detections. While the volcanological community has not reached consensus on the definition of the end of an eruption, for this discussion we define it as a return to background activity. As Raikoke does not have local

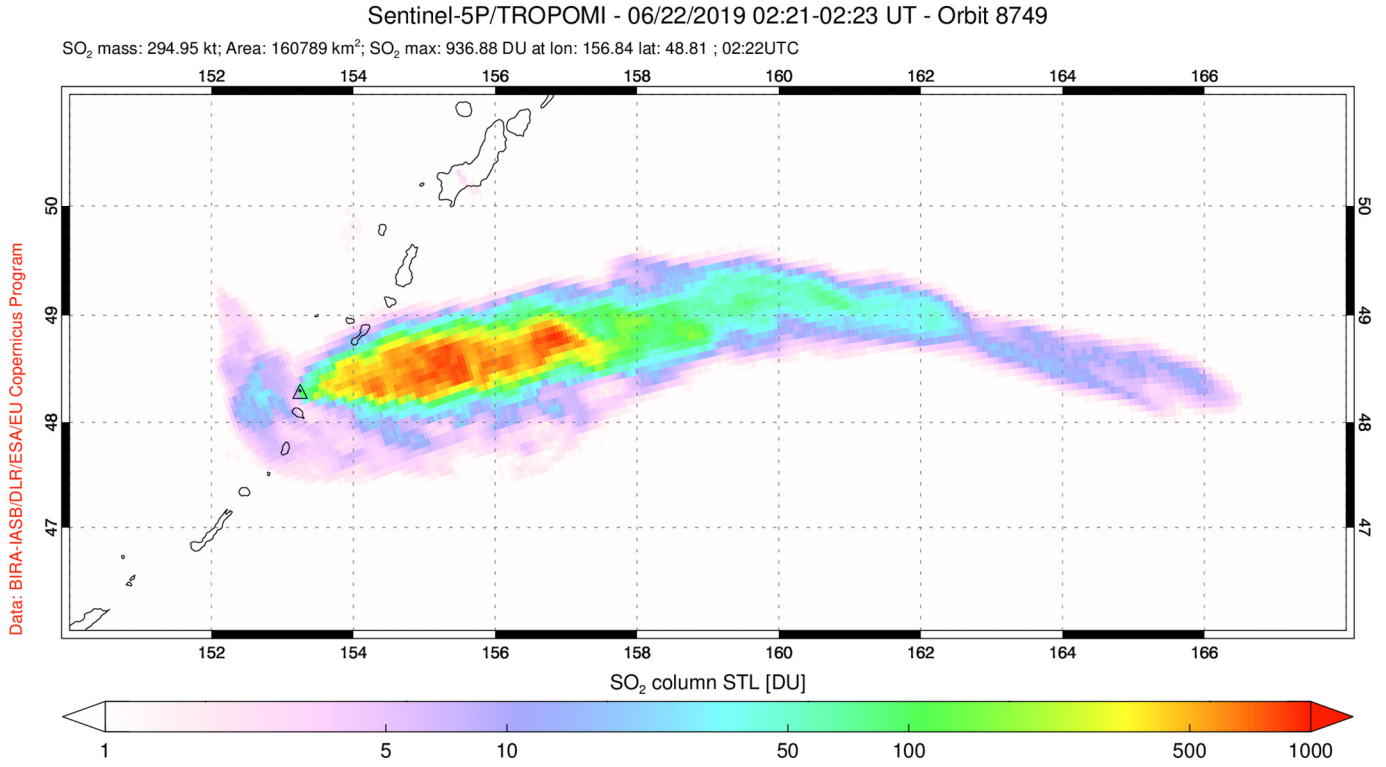

Fig. 8. Lower stratospheric (STL) SO_2 column amounts (in Dobson Units [DU]; 1 DU = 2.68×10^{16} molecules/cm^2) in the Raikoke eruption cloud, measured by S5P/TROPOMI at ~02:20 UTC on June 22. The total SO_2 mass measured at this time was ~0.3 Tg, but this is an underestimate of the actual SO_2 loading due to volcanic ash interference.

instrumentation, background activity level is no infrasound, lightning, deformation, or outgassing detected remotely. The eruption fell below detection limits on 22 June at about 8:15 UTC, marking a return to background activity. However, as with precursory unrest, there was likely lower level activity at the end of the eruptive sequence that was below the detection limits of remote tools.

We can resolve the change in island size and shape as well as the increase in crater area. We also document the likely eruption-induced algal bloom. While the RADARSAT-2 amplitude data captured the increase in island size, it clearly shows the widening of the crater rim to the north. However, the western rim is not discernible, resulting in a qualitative documentation.

In gathering and analyzing the data for this eruption common challenges arose. Issues we ran into included satellite and infrasound latency, cloud cover, and data access. The small island footprint made deformation harder to detect and characterize. Raikoke may not have deformed, the deformation may not have been detectable, or it could have been a relatively rapid precursory sequence. The closed system also meant precursory thermal and gas emissions were negligible or the signals were not within satellite resolution. In Table 1, we show the data we used for each phase of the eruption with bolded data denoting those that are classified as FAIR–Findable, Accessible, Interoperable, Reusable. We find that with FAIR data the eruption is detectible and broad characterization is feasible, especially since MODIS acquisition timing was favorable thus providing several plume height estimates. The additional data filled in details, particularly for syn-eruptive variations in lightning rate, current, and location, infrasound frequency and intensity changes, and higher resolution (every 10 min) thermal data for comparing plume heights and MER estimates to lightning and infrasound variations.

We also note that other systems exist to characterize volcanic unrest in real time using satellite observations. An example of this is VOLCAT (Pavolonis et al., 2018). The VOLCAT system is operated by NOAA/CIMSS and analyzes satellite data in real time to detect volcanic activity and provide alerts (Pavolonis et al., 2018). For the Raikoke 2019 eruption analyzed here, we find the majority of the VOLCAT ash heights from the alerts are comparable to the plume heights that are calculated in this manuscript, with the only exception being at 03:10 UTC. Here, VOLCAT determines a plume height of 20.2 km a.s.l. from the Aqua MODIS satellite, which is much higher than the height of ~10 km that we estimated for this time. This discrepancy would also lead to a much higher MER estimate. As there are no errors associated with this height, it is not used to subsequently determine a MER using the Monte Carlo modeling approach. We note that such a large difference in plume height would result in orders of magnitude difference when the Mastin relationship of plume height to MER is used (~1×10^5 kg/s from this study vrs. ~3×10^7 kg/s based on VOLCAT height) (Mastin et al., 2009).

By comparison to an identical study of an open-system eruption in Part II (McKee et al., this volume), we assess the relative strengths of remote sensing in application to closed- and open-system eruptions. For the closed-system case, the strength in remote observation was during the eruption, particularly the onset was very clear as infrasound, lightning, and ash plume detections started within minutes of each other then tracked the eruption as it pulsed and shifted to the main Plinian phase. The eruptive phases are unambiguous due to the temporal and spatial resolution gained from combining lightning, infrasound, and satellite remote sensing. As shown and discussed in McKee et al., (this volume), the onset of the open-system eruption was less clear as infrasound and gas emissions were detected prior to ash detections. Detection of precursory thermal and gas activity remains a challenge as closed systems emit little to no gas. Detecting deformation prior to eruption was a challenge in the case of Raikoke due to its dimensions. Post-eruptive changes were well documented in comparing pre- and post-eruption satellite imagery in both the closed- and open-systems. In sum, this was a fairly rapid eruption with clearly distinct phases and subtle if any precursors.

6. Conclusions

We characterized the 2019 VEI 4 eruption of Raikoke volcano using remote technologies (infrasound, lightning, and satellite remote

sensing) and plume modeling. Our analyses show six waxing pulses followed by the main Plinian phase and two subsequent waning pulses, which are well-documented by independent and strongly correlated infrasound, lightning, and ash plume observations. As the eruption moved into the main Plinian phase, the infrasound intensity, lightning stroke rate, and plume heights all increased. Additionally, the lightning duration corresponds to eruption duration as defined by the infrasound detections in the pulsatory phase. We also show that the lightning strokes with the highest estimated peak current occur closer to the vent and that stroke locations during the main Plinian phase follow the plume as it moves with the wind. Satellite remote sensing observations captured morphological changes from the eruption. We show an increase in the island and crater area resulting from tephra deposition and crater erosion, respectively. We did not detect precursory unrest with remote observational tools, but this is not out of the ordinary as Raikoke volcano is a closed system and the island size limited InSAR techniques. We illustrate the importance of an interdisciplinary approach to remote eruption characterization.

Data access

Local radiosonde and ERA-Interim reanalysis modelled data available at http://weather.uwyo.edu/. Both ASTER and MODIS data are openly available at several locations online including NASA Earthdata Search (https://search.earthdata.nasa.gov/search) and the U.S. Geological Survey EarthExplorer (https://earthexplorer.usgs.gov/). All Sentinel-2 data we use in this study are openly available at the Sentinel-hub EO-Browser (https://www.sentinel-hub.com/explore/eobrowser). Data from the CTBT IMS infrasound network are available through the CTBTO vDEC platform (https://www.ctbto.org/specials/vdec/). GLD360 data is available by request of Vaisala Inc. The International Space Station photograph is archived at the Gateway to Astronaut Photography of Earth (https://eol.jsc.nasa.gov/SearchPhotos/photo.pl?mission=ISS059&roll=E&frame=119250).

Declaration of Competing Interest

The authors declare that they have no known competing financial interests or personal relationships that could have appeared to influence the work reported in this paper.

Acknowledgements

This project originated at the Cooperative Institute for Dynamic Earth Research (CIDER) 2019 Summer Program: Volcanoes funded by NSF Grant EAR-1664595 to Bruce Buffett, Barbara Romanowicz, Roland Burgmann, Michael Manga, and Richard Allen. Judit Gonzalez Santana helped collect SAR data. Mike Poland processed SAR data. We thank John Stix, Dave Schneider, and an anonymous reviewer for helpful comments. Disclaimer: The views presented in this work are those of the authors and do not necessarily represent the views of the CTBTO. Maher, de Negri, and Matoza acknowledge NSF grants EAR-1620576 and EAR-1847736. McKee acknowledges NSF grant EAR-PF-1725730. Smith acknowledges NSF grant EAR-PF-1855153. Carn acknowledges NASA grants 80NSSC17K0240 and 80NSSC20K0983. Any use of trade, firm, or product names is for descriptive purposes only and does not imply endorsement by the U.S. Government. This work comprises Earth Observatory of Singapore contribution no. 357.

Appendix A. Supplementary data

Supplementary data to this article can be found online at https://doi.org/10.1016/j.jvolgeores.2021.107354.

References

Aizawa, K., Yokoo, A., Kanda, W., Ogawa, Y., Iguchi, M., 2010. Magnetotelluric pulses generated by volcanic lightning at Sakurajima volcano, Japan. Geophys. Res. Lett. 37. https://doi.org/10.1029/2010GL044208.

Aplin, K., Nicoll, K., Houghton, I., 2014. Electrical Charging of Volcanic Ash, in: Proc ESA Annual Meeting on Electrostatics.

Arason, P., Bennett, A.J., Burgin, L.E., 2011. Charge mechanism of volcanic lightning revealed during the 2010 eruption of Eyjafjallajökull. J. Geophys. Res. 116, 5315–5355. https://doi.org/10.1029/2011JB008651.

Armon, R.H., Starosvetsky, J., 2015. Algal Bloom Indicators. In: Armon, R.H., Hänninen, O. (Eds.), Environmental Indicators. Springer Netherlands, Dordrecht, pp. 633–642 https://doi.org/10.1007/978-94-017-9499-2_36.

Arnold, D.W.D., Biggs, J., Wadge, G., Mothes, P., 2018. Using satellite radar amplitude imaging for monitoring syn-eruptive changes in surface morphology at an ice-capped stratovolcano. Remote Sens. Environ. 209, 480–488. https://doi.org/10.1016/j.rse.2018.02.040.

Asrar, G., 1989. Theory and Applications of Optical Remote Sensing.

Bedard Jr., A.J., Georges, T.M., 2000. Atmospheric infrasound. Phys. Today 28, 32–37.

Behnke, S.A., McNutt, S.R., 2014. Using lightning observations as a volcanic eruption monitoring tool. Bull. Volcanol. 76, 112–193. https://doi.org/10.1007/s00445-014-0847-1.

Behnke, S.A., Thomas, R.J., McNutt, S.R., Schneider, D.J., Krehbiel, P.R., Rison, W., Edens, H.E., 2013. Observations of volcanic lightning during the 2009 eruption of Redoubt Volcano. J. Volcanol. Geotherm. Res. 259, 214–234. https://doi.org/10.1016/j.jvolgeores.2011.12.010.

Behnke, S.A., Thomas, R.J., Edens, H.E., Krehbiel, P.R., Rison, W., 2014. The 2010 eruption of Eyjafjallajökull: lightning and plume charge structure. J. Geophys. Res. 119, 833–859. https://doi.org/10.1002/2013JD020781.

Berrisford, P., Dee, D., Poli, P., Brugge, R., Fielding, K., Fuentes, M., Kallberg, P., Kobayashi, S., Uppala, S., Simmons, A., 2011. The ERA-Interim Archive, version 2.0.

Bessho, K., Date, K., Hayashi, M., Ikeda, A., Imai, T., Inoue, H., Kumagai, Y., Miyakawa, T., Murata, H., Ohno, T., Okuyama, A., Oyama, R., Sasaki, Y., Shimazu, Y., Shimoji, K., Sumida, Y., Suzuki, M., Taniguchi, H., Tsuchiyama, H., Uesawa, D., Yokota, H., Yoshida, R., 2016. An introduction to Himawari-8/9-Japan's new-generation geostationary meteorological satellites. J. Meteorol. Soc. Jpn. Ser II 94, 151–183. https://doi.org/10.2151/jmsj.2016-009.

Brown, D., Ceranna, L., Prior, M., Mialle, P., Le Bras, R.J., 2014. The IDC seismic, hydroacoustic and infrasound global low and high noise models. Pure Appl. Geophys. 171, 361–375. https://doi.org/10.1007/s00024-012-0573-6.

Bursik, M., 2001. Effect of wind on the rise height of volcanic plumes. Geophys. Res. Lett. 28, 3621–3624. https://doi.org/10.1029/2001GL013393.

Cannata, A., Montalto, P., Privitera, E., Russo, G., 2009. Characterization and location of infrasonic sources in active volcanoes: Mount Etna, September-November 2007. J. Geophys. Res. 114, B08308–B08315. https://doi.org/10.1029/2008JB006007.

Cansi, Y., 1995. An automatic seismic event processing for detection and location: the P.M.C.C. method. Geophys. Res. Lett. 22, 1021–1024. https://doi.org/10.1029/95GL00468.

Carlson, T.N., Ripley, D.A., 1997. On the relation between NDVI, fractional vegetation cover, and leaf area index. Remote Sens. Environ. 62, 241–252. https://doi.org/10.1016/S0034-4257(97)00104-1.

Carn, S.A., Clarisse, L., Prata, A.J., 2016. Multi-decadal satellite measurements of global volcanic degassing. J. Volcanol. Geotherm. Res. 311, 99–134. https://doi.org/10.1016/j.jvolgeores.2016.01.002.

Carn, S.A., Fioletov, V.E., Mclinden, C.A., Li, C., Krotkov, N.A., 2017. A decade of global volcanic SO2 emissions measured from space. Sci. Rep. 7, 1–12. https://doi.org/10.1038/srep44095.

Chaussard, E., Amelung, F., Aoki, Y., 2013. Characterization of open and closed volcanic systems in Indonesia and Mexico using InSAR time series. Solid J. Geophys. Res. Earth 118, 3957–3969. https://doi.org/10.1002/jgrb.50288.

Christie, D.R., Campus, P., 2010. The IMS Infrasound Network: Design and Establishment of Infrasound Stations, in: Infrasound Monitoring for Atmospheric Studies. Springer Netherlands, Dordrecht, pp. 29–75 https://doi.org/10.1007/978-1-4020-9508-5_2.

Cimarelli, C., Alatorre-Ibargüengoitia, M.A., Aizawa, K., Yokoo, A., Díaz-Marina, A., Iguchi, M., Dingwell, D.B., 2016. Multiparametric observation of volcanic lightning: Sakurajima Volcano, Japan. Geophys. Res. Lett. 43, 4221–4228. https://doi.org/10.1002/2015GL067445.

Cioni, R., Pistolesi, M., Rosi, M., 2015. Plinian and Subplinian Eruptions. Second ed. The Encyclopedia of Volcanoes. Elsevier Inc. https://doi.org/10.1016/b978-0-12-385938-9.00029-8.

Coombs, M.L., Wech, A.G., Haney, M.M., Lyons, J.J., Schneider, D.J., Schwaiger, H.F., Wallace, K.L., Fee, D., Freymueller, J.T., Schaefer, J.R., Tepp, G., 2018. Short-Term Forecasting and Detection of Explosions During the 2016–2017 Eruption of Bogoslof Volcano. Alaska. Front. Earth Sci. 6, 122. https://doi.org/10.3389/feart.2018.00122.

Coppola, D., Laiolo, M., Cigolini, C., Donne, D.D., Ripepe, M., 2016. Enhanced volcanic hotspot detection using MODIS IR data: results from the MIROVA system. Geol. Soc. Lond. Spec. Publ. 426, 181–205. https://doi.org/10.1144/SP426.5.

Corradini, S., Guerrieri, L., Lombardo, V., Merucci, L., Musacchio, M., Prestifilippo, M., Scollo, S., Silvestri, M., Spata, G., Stelitano, D., 2018. Proximal monitoring of the 2011–2015 Etna Lava fountains using MSG-SEVIRI data. Geosciences 8, 140. https://doi.org/10.3390/geosciences8040140.

Dabrowa, A.L., Green, D.N., Rust, A.C., Phillips, J.C., 2011. A global study of volcanic infrasound characteristics and the potential for long-range monitoring. Earth Planet. Sci. Lett. 310, 369–379. https://doi.org/10.1016/j.epsl.2011.08.027.

de Leeuw, J., Schmidt, A., Witham, C.S., Theys, N., Taylor, I.A., Grainger, R.G., Pope, R.J., Haywood, J., Osborne, M., Kristiansen, N.I., 2020. The 2019 Raikoke volcanic eruption:

Part 1 Dispersion model simulations and satellite retrievals of volcanic sulfur dioxide. Atmos. Chem. Phys. Discuss., 1–38. https://doi.org/10.5194/acp-2020-889.

Dee, D.P., Uppala, S.M., Simmons, A.J., Berrisford, P., Poli, P., Kobayashi, S., Andrae, U., Balmaseda, M.A., Balsamo, G., Bauer, P., Bechtold, P., Beljaars, A.C.M., van de Berg, L., Bidlot, J., Bormann, N., Delsol, C., Dragani, R., Fuentes, M., Geer, A.J., Haimberger, L., Healy, S.B., Hersbach, H., Hólm, E.V., Isaksen, L., Kaallberg, P., Köhler, M., Matricardi, M., McNally, A.P., Monge-Sanz, B.M., Morcrette, J.-J., Park, B.-K., Peubey, C., de Rosnay, P., Tavolato, C., Thépaut, J.-N., Vitart, F., 2011. The ERA-Interim reanalysis: configuration and performance of the data assimilation system. Q. J. R. Meteorol. Soc. 137, 553–597. https://doi.org/10.1002/qj.828.

Degruyter, W., Bonadonna, C., 2012. Improving on mass flow rate estimates of volcanic eruptions. Geophys. Res. Lett. 39. https://doi.org/10.1029/2012GL052566.

Degtyarev and Chibisova, 2019 A.V. Degtyarev, M.V. Chibisova The eruption of Raikokevolcano in June of 2019 (Raikoke Island, Central Kuril Islands)Geosyst. Transit. Zo., 3 (2019), pp. 304-309.

Devenish, B.J., Rooney, G.G., Webster, H.N., Thomson, D.J., 2010. The entrainment rate for Buoyant Plumes in a crossflow. Bound.-Layer Meteorol. 134, 411–439. https://doi.org/10.1007/s10546-009-9464-5.

Di Traglia, F., Nolesini, T., Solari, L., Ciampalini, A., Frodella, W., Steri, D., Allotta, B., Rindi, A., Marini, L., Monni, N., Galardi, E., Casagli, N., 2018. Lava delta deformation as a proxy for submarine slope instability. Earth Planet. Sci. Lett. 488, 46–58. https://doi.org/10.1016/j.epsl.2018.01.038.

Dietterich, H.R., Poland, M.P., Schmidt, D.A., Cashman, K.V., Sherrod, D.R., Espinosa, A.T., 2012. Tracking lava flow emplacement on the east rift zone of Kilauea, Hawai'i, with synthetic aperture radar coherence. Geochem. Geophys. Geosyst. 13, Q05001. https://doi.org/10.1029/2011GC004016.

Drusch, M., Del Bello, U., Carlier, S., Colin, O., Fernandez, V., Gascon, F., Hoersch, B., Isola, C., Laberinti, P., Martimort, P., Meygret, A., Spoto, F., Sy, O., Marchese, F., Bargellini, P., 2012. Sentinel-2: ESA's optical high-resolution mission for GMES operational services. Remote Sens. Environ. 120, 25–36. https://doi.org/10.1016/j.rse.2011.11.026.

Dwyer, J.R., Uman, M.A., 2014. The physics of lightning. Phys. Rep. 534, 147–241. https://doi.org/10.1016/j.physrep.2013.09.004.

Fee, D., Matoza, R.S., 2013. An overview of volcano infrasound: from hawaiian to plinian, local to global. J. Volcanol. Geotherm. Res. 249, 123–139. https://doi.org/10.1016/j.jvolgeores.2012.09.002.

Fee, D., Garcés, M., Steffke, A., 2010a. Infrasound from tungurahua volcano 2006–2008: strombolian to Plinian eruptive activity. J. Volcanol. Geotherm. Res. 193, 67–81. https://doi.org/10.1016/j.jvolgeores.2010.03.006.

Fee, D., Steffke, A., Garcés, M., 2010b. Characterization of the 2008 Kasatochi and Okmok eruptions using remote infrasound arrays. J. Geophys. Res. 115. https://doi.org/10.1029/2009jd013621 D00L10-15.

Fee, D., Matoza, R.S., Gee, K.L., Neilsen, T.B., Ogden, D.E., 2013a. Infrasonic crackle and supersonic jet noise from the eruption of Nabro Volcano, Eritrea. Geophys. Res. Lett. 40, 4199–4203. https://doi.org/10.1002/grl.50827.

Fee, D., McNutt, S.R., Lopez, T.M., Arnoult, K.M., Szuberla, C.A.L., Olson, J.V., 2013b. Combining local and remote infrasound recordings from the 2009 Redoubt Volcano eruption. J. Volcanol. Geotherm. Res. 259, 100–114. https://doi.org/10.1016/j.jvolgeores.2011.09.012.

Fee, D., Haney, M.M., Matoza, R.S., Van Eaton, A.R., Cervelli, P., Schneider, D.J., Iezzi, A.M., 2017. Volcanic tremor and plume height hysteresis from Pavlof Volcano, Alaska. Science 355, 45–48. https://doi.org/10.1126/science.aah6108.

Firstov, P.P., Popov, O.E., Lobacheva, M.A., Budilov, D.I., Akbashev, R.R., 2020. Wave perturbations in the atmosphere accompanying the eruption of the Raykoke volcano (Kuril Islands) June 21–22, 2019. Geosyst. Transit. Zones 4, 82–92. https://doi.org/10.30730/2541-8912.2020.4.1.071-081.082-092.

Forward, K.M., Lacks, D.J., Sankaran, R.M., 2009. Charge segregation depends on particle size in triboelectrically charged granular materials. Phys. Rev. Lett. 102, 028001. https://doi.org/10.1103/PhysRevLett.102.028001.

Genareau, K., Wallace, K.L., Gharghabi, P., Gafford, J., 2019. Lightning effects on the grain size distribution of Volcanic Ash. Geophys. Res. Lett. 1–14.

Genin, A., Lazar, B., Brenner, S., 1995. Vertical mixing and coral death in the red sea following the eruption of Mount Pinatubo. Nature 377, 507–510. https://doi.org/10.1038/377507a0.

Gillespie, A., Rokugawa, S., Matsunaga, T., Cothern, J.S., Hook, S., Kahle, A.B., 1998. A temperature and emissivity separation algorithm for Advanced Spaceborne Thermal Emission and Reflection Radiometer (ASTER) images. IEEE Trans. Geosci. Remote Sens. 36, 1113–1126. https://doi.org/10.1109/36.700995.

Girina, O.A., Loupian, E.A., Uvarov, I.A., Kramareva, L.S., 2019. Raikoke volcano eruption on 21 June 2019 [In Russian]. Sovrem. Probl. distantsionnogo Zo. Zemli iz kosmosa 16, 303–307. https://doi.org/10.21046/2070-7401-2019-16-3-303-307.

Glaze, L.S., Baloga, S.M., Wilson, L., 1997. Transport of atmospheric water vapor by volcanic eruption columns. J. Geophys. Res.-Atmos. 102, 6099–6108. https://doi.org/10.1029/96JD03125.

Gorshkov, G.S., 1970. Structure of the Kurile Arc. Volcanism and the Upper Mantle. Springer US, Boston, MA, pp. 1–6 https://doi.org/10.1007/978-1-4684-1767-8_1.

Haney, M.M., Van Eaton, A.R., Lyons, J.J., Kramer, R.L., Fee, D., Iezzi, A.M., 2018. Volcanic thunder from explosive eruptions at Bogoslof Volcano, Alaska. Geophys. Res. Lett. 45, 3429–3435.

Hargie, K.A., Van Eaton, A.R., Mastin, L.G., Holzworth, R.H., Ewert, J.W., Pavolonis, M., 2019. Globally detected volcanic lightning and umbrella dynamics during the 2014 eruption of Kelud, Indonesia. J. Volcanol. Geotherm. Res. 382, 81–91. https://doi.org/10.1016/j.jvolgeores.2018.10.016.

Hoblitt, R.P., 1994. An experiment to detect and locate lightning associated with eruptions of Redoubt Volcano. J. Volcanol. Geotherm. Res. 62, 499–517.

Holasek, R.E., Self, S., 1995. GOES weather satellite observations and measurements of the May 18, 1980, Mount St. Helens eruption. J. Geophys. Res. Solid Earth 100, 8469–8487. https://doi.org/10.1029/94JB03137.

Holasek, R.E., Self, S., Woods, A.W., 1996. Satellite observations and interpretation of the 1991 Mount Pinatubo eruption plumes. J. Geophys. Res. Solid Earth 101, 27635–27655. https://doi.org/10.1029/96JB01179.

Holdsworth, G., Peake, E., 1985. Acid content of snow from a mid-troposphere sampling site on Mount Logan, Yukon Territory, Canada. Ann. Glaciol. 7, 153–160. https://doi.org/10.3189/S0260305500006091.

Hooper, A., Zebker, H., Segall, P., Kampes, B., 2004. A new method for measuring deformation on volcanoes and other natural terrains using InSAR persistent scatterers. Geophys. Res. Lett. 31, L23611. https://doi.org/10.1029/2004GL021737.

Houghton, I.M.P., Aplin, K.L., Nicoll, K.A., 2013a. Triboelectric charging of volcanic ash from the 2011 Grímsvötn Eruption. Phys. Rev. Lett. 111, 118501. https://doi.org/10.1103/PhysRevLett.111.118501.

Houghton, B., Swanson, D.A., Rausch, J., Carey, R.J., Fagents, S.A., Orr, T.R., 2013b. Pushing the Volcanic Explosivity Index to its limit and beyond: constraints from exceptionally weak explosive eruptions at Kīlauea in 2008. Geology 41, 627–630. https://doi.org/10.1130/G34146.1.

Hoult, D.P., Weil, J.C., 1972. Turbulent plume in a laminar cross flow. Atmos. Environ. 1967 (6), 513–531. https://doi.org/10.1016/0004-6981(72)90069-8.

James, M.R., Lane, S.J., Gilbert, J.S., 2000. Volcanic plume electrification: experimental investigation of a fracture-charging mechanism. J. Geophys. Res. Solid Earth 105, 16641–16649. https://doi.org/10.1029/2000JB900068.

James, M.R., Wilson, L., Lane, S.J., Gilbert, J.S., Mather, T.A., Harrison, R.G., Martin, R.S., 2008. Electrical charging of volcanic plumes. Space Sci. Rev. 137, 399–418.

Johnson, J.B., Ruiz, M.C., Ortiz, H.D., Watson, L.M., Viracucha, G., Ramon, P., Almeida, M., 2018. Infrasound tornillos produced by Volcán Cotopaxi's Deep Crater. Geophys. Res. Lett. 45, 5436–5444. https://doi.org/10.1029/2018GL077766.

Kim, K.B., Jung, M.-K., Tsang, Y.F., Kwon, H.-H., 2020. Stochastic modeling of chlorophyll-a for probabilistic assessment and monitoring of algae blooms in the Lower Nakdong River, South Korea. J. Hazard. Mater. 400, 123066. https://doi.org/10.1016/j.jhazmat.2020.123066.

Lee, D.-C., Olson, J.V., Szuberla, C.A.L., 2013. Computationally robust and noise resistant numerical detector for the detection of atmospheric infrasound. J. Acoust. Soc. Am. 134, 862–868. https://doi.org/10.1121/1.4807802.

Li, C., Krotkov, N.A., Carn, S., Zhang, Y., Spurr, R.J., Joiner, J., 2017. New-generation NASA Aura Ozone Monitoring Instrument (OMI) volcanic SO 2 dataset: algorithm description, initial results, and continuation with the Suomi-NPP Ozone Mapping and Profiler Suite (OMPS). Atmospheric Meas. Tech. 10, 445. https://doi.org/10.5194/amt-10-445-2017.

Lindenthal, A., Langmann, B., Pätsch, J., Lorkowski, I., Hort, M., 2013. The ocean response to volcanic iron fertilisation after the eruption of Kasatochi volcano: A regional-scale biogeochemical ocean model study. Biogeosciences 10, 3715–3729. https://doi.org/10.5194/bg-10-3715-2013.

Lu, Z., Rykhus, R., Masterlark, T., Dean, K.G., 2004. Mapping recent lavaflows at Westdahl Volcano, Alaska, using radar and optical satellite imagery. Remote Sens. Environ. 91, 345–353. https://doi.org/10.1016/j.rse.2004.03.015.

Lyons, W.B., Mayewski, P.A., Spencer, M.J., Twickler, M.S., Graedel, T.E., 1990. A northern hemisphere volcanic chemistry record (1869–1984) and climatic implications using a south Greenland Ice Core. Ann. Glaciol. 14, 176–182. https://doi.org/10.3189/S0260305500008521.

Mantas, V.M., Pereira, A.J.S.C., Morais, P.V., 2011. Plumes of discolored water of volcanic origin and possible implications for algal communities. The case of the Home Reef eruption of 2006 (Tonga, Southwest Pacific Ocean). Remote Sens. Environ. 115, 1341–1352. https://doi.org/10.1016/j.rse.2011.01.014.

Marchetti, E., Ripepe, M., Harris, A.J.L., Delle Donne, D., 2009. Tracing the differences between Vulcanian and Strombolian explosions using infrasonic and thermal radiation energy. Earth Planet. Sci. Lett. 279, 273–281. https://doi.org/10.1016/j.epsl.2009.01.004.

Mastin, L.G., 2007. A user-friendly one-dimensional model for wet volcanic plumes. Geochem. Geophys. Geosyst. 8. https://doi.org/10.1029/2006GC001455.

Mastin, L.G., Guffanti, M., Servranckx, R., Webley, P., Barsotti, S., Dean, K., Durant, A., Ewert, J.W., Neri, A., Rose, W.I., Schneider, D., Siebert, L., Stunder, B., Swanson, G., Tupper, A., Volentik, A., Waythomas, C.F., 2009. A multidisciplinary effort to assign realistic source parameters to models of volcanic ash-cloud transport and dispersion during eruptions. J. Volcanol. Geotherm. Res. 186, 10–21. https://doi.org/10.1016/j.jvolgeores.2009.01.008.

Mastin, L.G., 2014. Testing the accuracy of a 1-D volcanic plume model in estimating mass eruption rate. J. Geophys. Res. Atmos. 119, 2474–2495. https://doi.org/10.1002/2013JD020604.

Matoza, R.S., Fee, D., Garcés, M.A., Seiner, J.M., Ramón, P.A., Hedlin, M.A.H., 2009. Infrasonic jet noise from volcanic eruptions. Geophys. Res. Lett. 36. https://doi.org/10.1029/2008gl036486.

Matoza, R.S., Le Pichon, A., Vergoz, J., Herry, P., Lalande, J.-M., Lee, H., Che, I.-Y., Rybin, A., 2011. Infrasonic observations of the June 2009 Sarychev Peak eruption, Kuril Islands: implications for infrasonic monitoring of remote explosive volcanism. J. Volcanol. Geotherm. Res. 200, 35–48. https://doi.org/10.1016/j.jvolgeores.2010.11.022.

Matoza, R.S., Fee, D., Neilsen, T.B., Gee, K.L., Ogden, D.E., 2013a. Aeroacoustics of volcanic jets: acoustic power estimation and jet velocity dependence. J. Geophys. Res. Solid Earth 118, 6269–6284. https://doi.org/10.1002/2013JB010303.

Matoza, R.S., Landès, M., Le Pichon, A., Ceranna, L., Brown, D., 2013b. Coherent ambient infrasound recorded by the International Monitoring System. Geophys. Res. Lett. 40, 429–433. https://doi.org/10.1029/2012GL054329.

Matoza, R.S., Green, D.N., Le Pichon, A., Shearer, P.M., Fee, D., Mialle, P., Ceranna, L., 2017. Automated detection and cataloging of global explosive volcanism using the

International Monitoring System infrasound network. J. Geophys. Res. Solid Earth 122, 2946–2971. https://doi.org/10.1002/2016JB013356.
Matoza, R.S., Fee, D., Green, D.N., Le Pichon, A., Vergoz, J., Haney, M.M., Mikesell, T.D., Franco, L., Valderrama, O.A., Kelley, M.R., McKee, K., Ceranna, L., 2018. Local, regional, and remote seismo-acoustic observations of the April 2015 VEI 4 eruption of Calbuco Volcano, Chile. J. Geophys. Res. Solid Earth 123, 3814–3827. https://doi.org/10.1002/2017JB015182.
Matoza, R., Fee, D., Green, D., Mialle, P., 2019. Volcano infrasound and the international monitoring System. In: Le Pichon, A., Blanc, E., Hauchecorne, A. (Eds.), Infrasound Monitoring for Atmospheric Studies. Springer International Publishing, Cham, pp. 1023–1077 https://doi.org/10.1007/978-3-319-75140-5_33.
McGimsey, R.G., Neal, C.A., Girina, O.A., Chibisova, M.V., Rybin, A., 2014. 2009 Volcanic Activity in Alaska, Kamchatka, and the Kurile Islands — Summary of Events and Response of the Alaska Volcano Observatory Scientific Investigations Report. , pp. 2013–5213 https://doi.org/10.3133/sir20135213.
McNutt, S.R., Williams, E.R., 2010. Volcanic lightning: global observations and constraints on source mechanisms. Bull. Volcanol. 72, 1153–1167. https://doi.org/10.1007/s00445-010-0393-4.
Méndez Harper, J., Dufek, J., 2016. The effects of dynamics on the triboelectrification of volcanic ash. J. Geophys. Res. 121, 8209–8228. https://doi.org/10.1002/2015JD024275.
Miura, T., Koyaguchi, T., Tanaka, Y., 2002. Measurements of electric charge distribution in volcanic plumes at Sakurajima Volcano, Japan. Bull. Volcanol. 64, 75–93. https://doi.org/10.1007/s00445-001-0182-1.
Morton, B.R., Taylor, G.I., Turner, J.S., 1956. Turbulent gravitational convection from maintained and instantaneous sources. Proc. R. Soc. Lond. Ser. Math. Phys. Sci. 234, 1–23. https://doi.org/10.1098/rspa.1956.0011.
National Academies of Sciences, Engineering, Medicine, 2020. A Vision for NSF Earth Sciences 2020-2030: Earth in Time. National Academies Press, Washington, D.C. https://doi.org/10.17226/25761.
Newhall, C.G., Self, S., 1982. The volcanic explosivity index (VEI) an estimate of explosive magnitude for historical volcanism. J. Geophys. Res. 87, 1231. https://doi.org/10.1029/JC087iC02p01231.
Olson, J.V., Szuberla, C.A., 2008. Processing infrasonic array data. In: Havelock, D., Kuwano, S., Vorlander, M. (Eds.), Handbook of Signal Processing in Acoustics. Springer, New York, NY, pp. 1487–1496.
Oppenheimer, C., 1998. Review article: volcanological applications of meteorological satellites. Int. J. Remote Sens. 19, 2829–2864. https://doi.org/10.1080/014311698214307.
Pallister, J.S., Schneider, D.J., Griswold, J.P., Keeler, R.H., Burton, W.C., Noyles, C., Newhall, C.G., Ratdomopurbo, A., 2013. Merapi 2010 eruption-Chronology and extrusionrates monitored with satellite radar and used in eruption forecasting. J. Volcanol. Geotherm. Res. https://doi.org/10.1016/j.jvolgeores.2012.07.012.
Pavolonis, M.J., Sieglaff, J., Cintineo, J., 2018. Automated detection of explosive volcanic eruptions using satellite-derived cloud vertical growth rates. Earth Space Sci. 5, 903–928. https://doi.org/10.1029/2018EA000410.
Poland, M.P., Lopez, T., Wright, R., Pavolonis, M.J., 2020. Forecasting, detecting, and tracking volcanic eruptions from space. Remote Sens. Earth Syst. Sci. 3, 55–94. https://doi.org/10.1007/s41976-020-00034-x.
Prata, A.J., Grant, I.F., 2001. Retrieval of microphysical and morphological properties of volcanic ash plumes from satellite data: application to Mt Ruapehu, New Zealand. Q. J. R. Meteorol. Soc. 127, 2153–2179. https://doi.org/10.1002/qj.49712757615.
Prata, A.T., Folch, A., Prata, A.J., Biondi, R., Brenot, H., Cimarelli, C., Corradini, S., Lapierre, J., Costa, A., 2020. Anak Krakatau triggers volcanic freezer in the upper troposphere. Sci. Rep. 10, 3584. https://doi.org/10.1038/s41598-020-60465-w.
Pritchard, M.E., Simons, M., 2004. An InSAR-based survey of volcanic deformation in the central Andes. Geochem. Geophys. Geosyst. 5, Q02002. https://doi.org/10.1029/2003GC000610.
Pyle, D.M., 1989. The thickness, volume and grainsize of tephra fall deposits. Bull. Volcanol. 51, 1–15. https://doi.org/10.1007/BF01086757.
Pyle, D.M., 2015. Sizes of Volcanic Eruptions. Second ed. The Encyclopedia of Volcanoes. Elsevier Inc. https://doi.org/10.1016/b978-0-12-385938-9.00013-4.
Rashidov, V.A., Girina, O.A., Ozerov, A.Y., Pavlov, N.N., 2019. The june 2019 eruption of Raikoke volcano (the Kurile islands). Bull. Kamchatka Reg. Assoc. "Educational-Scientific center". Earth Sci. 42, 5–8. doi:10.31431/1816-5524-2019-2-42-5-8. http://www.kscnet.ru/journal/kraesc/article/view/243.
Reath, K., Pritchard, M., Poland, M., Delgado, F., Carn, S., Coppola, D., Andrews, B., Ebmeier, S.K., Rumpf, E., Henderson, S., Baker, S., Lundgren, P., Wright, R., Biggs, J., Lopez, T., Wauthier, C., Moruzzi, S., Alcott, A., Wessels, R., Griswold, J., Ogburn, S., Loughlin, S., Meyer, F., Vaughan, G., Bagnardi, M., 2019a. Thermal, deformation, and degassing remote sensing time series (CE 2000–2017) at the 47 most active Volcanoes in Latin America: implications for volcanic systems. J. Geophys. Res. Solid Earth 124, 195–218. https://doi.org/10.1029/2018JB016199.
Reath, K., Pritchard, M.E., Moruzzi, S., Alcott, A., Coppola, D., Pieri, D., 2019b. The AVTOD (ASTER Volcanic Thermal Output Database) Latin America archive. J. Volcanol. Geotherm. Res. 376, 62–74. https://doi.org/10.1016/j.jvolgeores.2019.03.019.
Riedel, K.S., Sidorenko, A., 1995. Minimum bias multiple taper spectral estimation. IEEE Trans. Signal Process. 43, 188–195. https://doi.org/10.1109/78.365298.
Sato, M., Hansen, J.E., McCormick, M.P., Pollack, J.B., 1993. Stratospheric aerosol optical depths, 1850–1990. J. Geophys. Res. 98, 22987. https://doi.org/10.1029/93JD02553.
Schneider, D.J., Hoblitt, R.P., 2013. Doppler weather radar observations of the 2009 eruption of Redoubt Volcano, Alaska. J. Volcanol. Geotherm. Res. 259, 133–144.
Smirnov, S.Z., Nizametdinov, I.R., Timina, T.Y., Kotov, A.A., Sekisova, V.S., Kuzmin, D.V., ... Abersteiner, A., 2021. High explosivity of the June 21, 2019 eruption of Raikoke volcano (Central Kuril Islands); mineralogical and petrological constraints on the pyroclastic materials. Journal of Volcanology and Geothermal Research 107346. https://doi.org/10.1016/j.jvolgeores.2021.107346.
Smith, C.M., Van Eaton, A.R., Charbonnier, S., McNutt, S.R., Behnke, S.A., Thomas, R.J., Edens, H.E., Thompson, G., 2018a. Correlating the electrification of volcanic plumes with ashfall textures at Sakurajima Volcano, Japan. Earth Planet. Sci. Lett. 492, 47–58. https://doi.org/10.1016/j.epsl.2018.03.052.
Smith, C.M., Van Eaton, A.R., Said, R., Holzworth, R.H., 2018b. Volcanic lightning as a monitoring tool during the 2016-2017 eruption of Bogoslof Volcano, AK. 25th International Lightning Detect Conference & 7th International Lightning Meteorology Conference, pp. 1–5.
Stall, S., Yarmey, L., Boehm, R., Cousijn, H., Cruse, P., Cutcher-Gershenfeld, J., Dasler, R., de Waard, A., Duerr, R., Elger, K., Fenner, M., Glaves, H., Hanson, B., Hausman, J., Heber, J., Hills, D., Hoebelheinrich, N., Hou, S., Kinkade, D., Koskela, R., Martin, R., Lehnert, K., Murphy, F., Nosek, B., Parsons, M., Petters, J., Plante, R., Robinson, E., Samors, R., Servilla, M., Ulrich, R., Witt, M., Wyborn, L., 2018. Advancing FAIR Data in Earth, Space, and Environmental Science. Eos 99 https://doi.org/10.1029/2018EO109301.
Suzuki, Y.J., Koyaguchi, T., 2009. A three-dimensional numerical simulation of spreading umbrella clouds. J. Geophys. Res. Solid Earth 114.
SVERT, 2009. Widespread plumes from large 11–16 June 2009 eruption. Bulletin of the Global Volcanism Network, Monthly Report 06/2009. Smithsonian Global Volcanism Program 34:06.
Taran, Y., Zelenski, M., Chaplygin, I., Malik, N., Campion, R., Inguaggiato, S., Pokrovsky, B., Kalacheva, E., Melnikov, D., Kazahaya, R., 2018. Gas emissions from volcanoes of the Kuril island arc (NW pacific): geochemistry and fluxes. Geochem. Geophys. Geosyst. 19, 1859–1880.
Tatarinov, M., 1785. Description of the Kurile Islands. Historical and Geographical Calendar for 1785 St. Petersburg.
Theys, N., Smedt, I.D., Yu, H., Danckaert, T., van Gent, J., Hörmann, C., Wagner, T., Hedelt, P., Bauer, H., Romahn, F., 2017. Sulfur dioxide retrievals from TROPOMI onboard Sentinel-5 Precursor: algorithm theoretical basis. Atmospheric Meas. Tech. 10.
Theys, N., Hedelt, P., De Smedt, I., Lerot, C., Yu, H., Vlietinck, J., Pedergnana, M., Arellano, S., Galle, B., Fernandez, D., 2019. Global monitoring of volcanic SO 2 degassing with unprecedented resolution from TROPOMI onboard Sentinel-5 Precursor. Sci. Rep. 9, 1–10.
Van Eaton, A.R., Amigo, Á., Bertin, D., Mastin, L.G., Giacosa, R.E., González, J., Valderrama, O., Fontijn, K., Behnke, S.A., 2016. Volcanic lightning and plume behavior reveal evolving hazards during the April 2015 eruption of Calbuco volcano, Chile. Geophys. Res. Lett. 43, 3563–3571. https://doi.org/10.1002/2016GL068076.
Van Eaton, A.R., Schneider, D.J., Smith, C.M., Haney, M.M., Lyons, J.J., Said, R., Fee, D., Holzworth, R.H., Mastin, L.G., 2020. Did ice-charging generate volcanic lightning during the 2016–2017 eruption of Bogoslof volcano, Alaska? Bull. Volcanol. 82, 24. https://doi.org/10.1007/s00445-019-1350-5.
van Stokkom, A., 2013. Algal Blooms Seasonality along the Coast of Iceland and Volcanic Influences from the Eyjafjallajökull Eruption in 2010. University of Iceland, Reykjavik, Iceland.
Veefkind, J.P., Aben, I., McMullan, K., Förster, H., de Vries, J., Otter, G., Claas, J., Eskes, H.J., de Haan, J.F., Kleipool, Q., van Weele, M., Hasekamp, O., Hoogeveen, R., Landgraf, J., Snel, R., Tol, P., Ingmann, P., Voors, R., Kruizinga, B., Vink, R., Visser, H., Levelt, P.F., 2012. TROPOMI on the ESA Sentinel-5 Precursor: a GMES mission for global observations of the atmospheric composition for climate, air quality and ozone layer applications. Remote Sens. Environ. 120, 70–83. https://doi.org/10.1016/j.rse.2011.09.027.
Wadge, G., Saunders, S., Itikarai, I., 2012. Pulsatory andesite lava flow at Bagana Volcano. Geochem. Geophys. Geosyst. 13, Q11011. https://doi.org/10.1029/2012GC004336.
Walker, G.P.L., 1973. Explosive volcanic eruptions — a new classification scheme. Geol. Rundsch. 62, 431–446. https://doi.org/10.1007/BF01840108.
Whitaker, R.W., Norris, D.E., 2008. Infrasound propagation. Handb. Signal Process. Acoust., 1497–1519 https://doi.org/10.1007/978-0-387-30441-0_82.
Wilkinson, M.D., Dumontier, M., Aalbersberg, Ij.J., Appleton, G., Axton, M., Baak, A., Blomberg, N., Boiten, J.-W., da Silva Santos, L.B., Bourne, P.E., Bouwman, J., Brookes, A.J., Clark, T., Crosas, M., Dillo, I., Dumon, O., Edmunds, S., Evelo, C.T., Finkers, R., Gonzalez-Beltran, A., Gray, A.J.G., Groth, P., Goble, C., Grethe, J.S., Heringa, J., 't Hoen, P.A.C., Hooft, R., Kuhn, T., Kok, R., Kok, J., Lusher, S.J., Martone, M.E., Mons, A., Packer, A.L., Persson, B., Rocca-Serra, P., Roos, M., van Schaik, R., Sansone, S.-A., Schultes, E., Sengstag, T., Slater, T., Strawn, G., Swertz, M.A., Thompson, M., van der Lei, J., van Mulligen, E., Velterop, J., Waagmeester, A., Wittenburg, P., Wolstencroft, K., Zhao, J., Mons, B., 2016. The FAIR Guiding Principles for scientific data management and stewardship. Sci. Data 3, 160018 https://doi.org/10.1038/sdata.2016.18.
Williams, E., Nathou, N., Hicks, E., Pontikis, C., Russell, B., Miller, M., Bartholomew, M.J., 2009. The electrification of dust-lofting gust fronts ('haboobs') in the Sahel. Atmos. Res. 91, 292–298. https://doi.org/10.1016/j.atmosres.2008.05.017.
Woodhouse, M.J., Behnke, S.A., 2014. Charge structure in volcanic plumes: a comparison of plume properties predicted by an integral plume model to observations of volcanic lightning during the 2010 eruption of Eyjafjallajökull. Iceland. Bull. Volcanol. 76, 1–21. https://doi.org/10.1007/s00445-014-0828-4.
Woods, A.W., 1993. A model of the plumes above basaltic fissure eruptions. Geophys. Res. Lett. 20, 1115–1118. https://doi.org/10.1029/93GL01215.
Woods, A.W., Self, S., 1992. Thermal disequilibrium at the top of volcanic clouds and its effect on estimates of the column height. Nature 355, 628–630. https://doi.org/10.1038/355628a0.
Wright, R., Flynn, L.P., Garbeil, H., Harris, A.J.L., Pilger, E., 2004. MODVOLC: near-real-time thermal monitoring of global volcanism. J. Volcanol. Geotherm. Res. 135, 29–49. https://doi.org/10.1016/j.jvolgeores.2003.12.008.
Zielinski, G.A., 1995. Stratospheric loading and optical depth estimates of explosive volcanism over the last 2100 years derived from the Greenland Ice Sheet Project 2 ice core. J. Geophys. Res. 100, 20937. https://doi.org/10.1029/95JD01751.